



IntelliO3-ts v1.0: a neural network approach to predict near-surface ozone concentrations in Germany

Felix Kleinert^{1,2}, Lukas H. Leufen^{1,2}, and Martin G. Schultz¹

¹Jülich Supercomputing Centre, Forschungszentrum Jülich, Jülich, Germany

²Institute of Geosciences, Rheinische Friedrich-Wilhelms-Universität Bonn, Bonn, Germany

Correspondence: Felix Kleinert (f.kleinert@fz-juelich.de)

Received: 3 June 2020 – Discussion started: 17 August 2020

Revised: 6 November 2020 – Accepted: 7 November 2020 – Published: 4 January 2021

Abstract. The prediction of near-surface ozone concentrations is important for supporting regulatory procedures for the protection of humans from high exposure to air pollution. In this study, we introduce a data-driven forecasting model named “IntelliO3-ts”, which consists of multiple convolutional neural network (CNN) layers, grouped together as inception blocks. The model is trained with measured multi-year ozone and nitrogen oxide concentrations of more than 300 German measurement stations in rural environments and six meteorological variables from the meteorological COSMO reanalysis. This is by far the most extensive dataset used for time series predictions based on neural networks so far. IntelliO3-ts allows the prediction of daily maximum 8 h average (dma8eu) ozone concentrations for a lead time of up to 4 d, and we show that the model outperforms standard reference models like persistence models. Moreover, we demonstrate that IntelliO3-ts outperforms climatological reference models for the first 2 d, while it does not add any genuine value for longer lead times. We attribute this to the limited deterministic information that is contained in the single-station time series training data. We applied a bootstrapping technique to analyse the influence of different input variables and found that the previous-day ozone concentrations are of major importance, followed by 2 m temperature. As we did not use any geographic information to train IntelliO3-ts in its current version and included no relation between stations, the influence of the horizontal wind components on the model performance is minimal. We expect that the inclusion of advection–diffusion terms in the model could improve results in future versions of our model.

1 Introduction

Exposure to ambient air pollutants such as ozone (O₃) is harmful for living beings (WHO, 2013; Bell et al., 2014; Lefohn et al., 2017; Fleming et al., 2018) and certain crops (Avnery et al., 2011; Mills et al., 2018). Therefore, the prediction of ozone concentrations is of major importance for issuing warnings for the public if high ozone concentrations are foreseeable. As tropospheric ozone is a secondary air pollutant, there is nearly no source of directly emitted ozone. Instead, it is formed in chemical reactions of several precursors like nitrogen oxides (NO_x) or volatile organic compounds (VOCs). Weather conditions (temperature, irradiation, humidity, and winds) have a major influence on the rates of ozone formation and destruction. Ozone has a “chemical lifetime” in the lower atmosphere of several days and can therefore be transported over distances of several hundred kilometres.

Ozone concentrations can be forecasted by various numerical methods. Chemical transport models (CTMs) solve chemical and physical equations explicitly (for example, Collins et al., 1997; Wang et al., 1998a, b; Horowitz et al., 2003; von Kuhlmann et al., 2003; Grell et al., 2005; Donner et al., 2011). These numerical models predict concentrations for grid cells, which are assumed to be representative of a given area. Therefore, local fluctuations which are below model resolution cannot be simulated. Moreover, CTMs often have a bias in concentrations, turnover rates, or meteorological properties which have a direct influence on chemical processes (Vautard, 2012; Brunner et al., 2015).

This makes CTMs unsuited for regulatory purposes, which by law are bound to station measurements, except if so-called

model output statistics are applied to the numerical modelling results (Fuentes and Raftery, 2005). As an alternative to CTMs, regression models are often used to generate point forecasts (for example, Olszyna et al., 1997; Thompson et al., 2001; Abdul-Wahab et al., 2005). Regression models are pure statistical models, which are based on empirical relations among different variables. They usually describe a linear functional relationship between various factors (precursor concentrations, meteorological, and site information) and the air pollutant in question.

Since the late 1990s, machine learning techniques in the form of neural networks have also been applied as a regression technique to forecast ozone concentrations or threshold value exceedances (see Table 1). As the computational power was limited in the early days of those approaches, many of these early studies focused on a small number of measurement stations and used a fully connected (FC) network architecture. More recent studies explored the use of more advanced network architectures like convolutional neural networks (CNNs) or long short-term memory (LSTM) networks. These networks were also applied to a larger number of stations compared to the earlier studies and some studies have tried to generalise, i.e. to train one neural network for all stations instead of training individual networks for individual stations (Table 1). Although the total number of studies focusing on air quality or explicit near-surface ozone is already quite substantial, there are only few studies which applied advanced deep learning approaches on a larger number of stations or on longer time series. Eslami et al. (2020) applied a CNN on time series of 25 measurement stations in Seoul, South Korea, to predict hourly ozone concentrations for the next 24 h. Ma et al. (2020) trained a bidirectional LSTM on 19 measurement sites over a period of roughly 9 months and afterwards used that model to re-train individually for 48 previously unused measurement stations (transfer learning).

Sayeed et al. (2020) applied a deep CNN on data from 21 different measurement stations over a period of 4 years. They used 3 years (2014 to 2016) to train their model and evaluated the generalisation capability on the fourth year (2017). Zhang et al. (2020) developed a hybrid CNN–LSTM model to predict gridded air quality concentrations (O_3 , NO_2 , CO , $\text{PM}_{2.5}$, PM_{10}). Seltzer et al. (2020) used 3557 measurement sites across six measurement networks to analyse long-term ozone exposure trends in North America by applying a fully connected neural network. They mainly focused on metrics related to human health and crop loss.

The current study extends these previous works and introduces a new deep learning model for the prediction of daily maximum 8 h average O_3 concentrations (dma8eu; see Sect. 2.1) for a lead time of up to 4 d. The network architecture is based on several stacks of convolutional neural networks. We trained our network with data from 312 background measurement stations in Germany (date range from 1997 to 2007) and tuned hyperparameters on data from 211

stations (data range from 2008 to 2009). We evaluate the performance at 203 stations, which have data during the 2010–2015 period looking at skill scores, the joint distribution of forecasts and observations, as well as the influence of input variables.

This article is structured as follows: in Sect. 2, we explain our variable selection and present our preprocessing steps. In Sect. 3, we introduce our forecasting model (IntelliO3-ts, version 1.0). Section 4 introduces the statistical tools and reference models which were used for verification. In Sect. 5, we present and discuss the results and analyse the influence of different input variables on the model performance. In Sect. 6, we discuss the limitations of IntelliO3-ts. Finally, Sect. 7 provides conclusions.

2 Variable selection and data processing

2.1 Variable selection

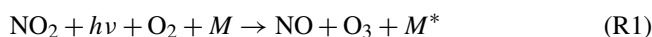
Tropospheric ozone (O_3) is a greenhouse gas formed in the atmosphere by chemical reactions of other directly emitted pollutants (ozone precursors) and therefore referred to as a secondary air pollutant.

The continuity equation of near-surface ozone in a specific volume of air can be written as (Jacobson, 2005, p. 74ff)

$$\frac{\partial N_q}{\partial t} + \nabla \cdot (\mathbf{v} N_q) = (\nabla \cdot \mathbf{K}_h \nabla) N_q + R_{\text{depg}} + R_{\text{chemg}}, \quad (1)$$

where $\frac{\partial N_q}{\partial t}$ is the partial derivative of the ozone number concentration with respect to time, \mathbf{v} is the vector wind velocity, \mathbf{K}_h is the eddy diffusion tensor for energy, while R_{depg} and R_{chemg} are the rates of dry deposition to the ground, and photochemical production or loss, respectively.

Tropospheric ozone is formed under sunlit conditions in gas-phase chemical reactions of peroxy radicals and nitrogen oxides (Seinfeld and Pandis, 2016). The peroxy radicals are themselves oxidation products of volatile organic compounds. The nitrogen oxides undergo a rapid catalytic cycle:



where NO and O_3 are converted to NO_2 and back within minutes (M is an arbitrary molecule which is needed to take up excess energy, denoted by the asterisk). As a consequence, ozone concentrations in urban areas with high levels of NO_x from combustive emissions are extremely variable. In this study, we therefore focus on background stations, which are less affected by the rapid chemical interconversion.

From a chemical perspective, the prediction of ozone concentrations would require concentration data of NO, NO_2 , speciated VOC, and O_3 itself. However, since speciated VOC measurements are only available from very few measurement sites, the chemical input variables of our model are limited to NO, NO_2 , and O_3 .

Table 1. Overview of the literature on ozone forecasts with neural networks. Machine learning (ML) types are abbreviated as FC for fully connected, CNN for convolutional neural network, RNN for recurrent neural network, and LSTM for long short-term memory. We use the following abbreviations for time periods: yr for years and m for month.

Citation	ML type	Total number of stations	Stations for training	Time period	Comments
Comrie (1997)	FC	8	8	5 yr	Random split for train, val
Cobourn et al. (2000)	FC	7	7	5 yr (train) + 1 yr (val) + 1 yr (test)	
Prybutok et al. (2000)	FC	1		4 m + 1 m	
Gardner and Dorling (2001)	FC	6	6	12 yr	
Eslami et al. (2020)	CNN	25	25	3 yr train 1 yr test	Random split
Liu et al. (2019)	Attention RNN	2	2	10 m (train), 7 d (test)	Analysis for PM _{2.5}
Maleki et al. (2019)	FC	4	4	1 yr	Random split for train, val, test
Silva et al. (2019)	FC	2	1	13 yr (train, val test); 14 yr (test on second station)	Dry deposition of O ₃ ; random split on first station
Abdul Aziz et al. (2019)	FC	1	1	7 d	Individual measurements for study
Pawlak and Jarosławski (2019)	FC	2	2	6 m (train) + 6 m (test)	Individual network per station
Seltzer et al. (2020)	FC	3557	3557	15 yr	focus on trends
Ma et al. (2020)	Bidir. LSTM	19 (standard) + 48 (transfer)	19 (standard) + 48 (transfer)	9 m	Exploration of transfer learning
Sayeed et al. (2020)	CNN	21	21	3 yr (train) + 1 yr (test/re-train)	Re-train model for each prediction
Zhang et al. (2020)	CNN LSTM	35	35	19 m	Gridded forecast
This study	Inception blocks	329	312	18 yr	

Besides the trace gas concentrations, ozone levels also depend on meteorological variables. Due to the scarcity of reported meteorological measurements at the air quality monitoring sites, we extracted time series of meteorological variables from the 6 km resolution COSMO reanalysis (Bollmeyer et al., 2015, COSMO-REA6) and treat those as observations.

All data used in this study were retrieved from the Tropospheric Ozone Assessment Report (TOAR) database (Schultz et al., 2017) via the representational state transfer (REST) application programming interface (API) at <https://join.fz-juelich.de> (last access: 12 November 2020). The air quality measurements were provided by the German Umweltbundesamt, while the meteorological data were extracted from the COSMO-REA6 reanalysis as described above. These reanalysis data cover the period from 1995 to 2015 with some gaps due to incompleteness in the TOAR database. As discussed in the US EPA guidelines on air quality forecasting (Dye, 2003), ozone concentrations typically depend on temperature, irradiation, humidity, wind speed, and wind direction. The vertical structure of the lowest portion of the atmosphere (i.e. the planetary boundary layer) also plays an important role, because it determines the rate of mixing between fresh pollution and background air. Since irradiation data were not available from the REST interface, we used cloud cover together with temperature as proxy variables.

Table 2 shows the list of input variables used in this study, and Table 3 describes the daily statistics that were applied to the hourly data of each variable. The choice of using the dma8eu metrics for NO and NO₂ was motivated by the idea

Table 2. Input variables and applied daily statistics according to Table 3.

Variable	Daily statistics
NO	dma8eu
NO ₂	dma8eu
O ₃	dma8eu
Cloud cover	average
Planetary boundary layer height	maximum
Relative humidity	average
Temperature	maximum
Wind's <i>u</i> component	average
Wind's <i>v</i> component	average

to sample all chemical quantities during the same time periods and with similar averaging times. While the dma8eu metrics is calculated based on data starting at 17:00 LT on the previous day, the daily mean/max values, for example, would be calculated based on data starting from the current day. To test the impact of using different metrics for ozone precursors, we also trained the model from scratch with either mean or maximum concentrations of NO and NO₂ as inputs. The results of these runs were hardly distinguishable from the results presented below.

As described above, ozone concentrations are less variable at stations, which are further away from primary pollutant emission sources. We therefore selected those stations from the German air quality monitoring network, which are labelled as “background” stations according to the European Environmental Agency (EEA), Airbase classification.

Table 3. Definitions of statistical metrics in TOAR analysis relevant for this study. Adopted from Schultz et al. (2017, Supplement 1, Table 6, therein).

Name	Description
data_capture	Fraction of valid (hourly) values available in the aggregation period.
average_values	Daily [...] average value. No data capture criterion is applied, i.e. a daily average is valid if at least one hourly value of the day is present.
dma8eu	As dma8epa but using the EU definition of the daily 8 h window starting from 17:00 LT of the previous day. (dma8epa: daily maximum 8 h average statistics according to the US EPA definition. The 8 h averages are calculated for 24 bins starting at 00:00 LT. The 8 h running mean for a particular hour is calculated on the concentration for that hour plus the following 7 h. If less than 75 % of data are present (i.e. less than 6 h), the average is considered missing. Note that in contrast to the official EPA definition, a daily value is considered valid if at least one 8 h average is valid.)
maximum	Daily maximum value. No data capture criterion is applied; i.e. a daily maximum is valid if at least one hourly value of the day is present.

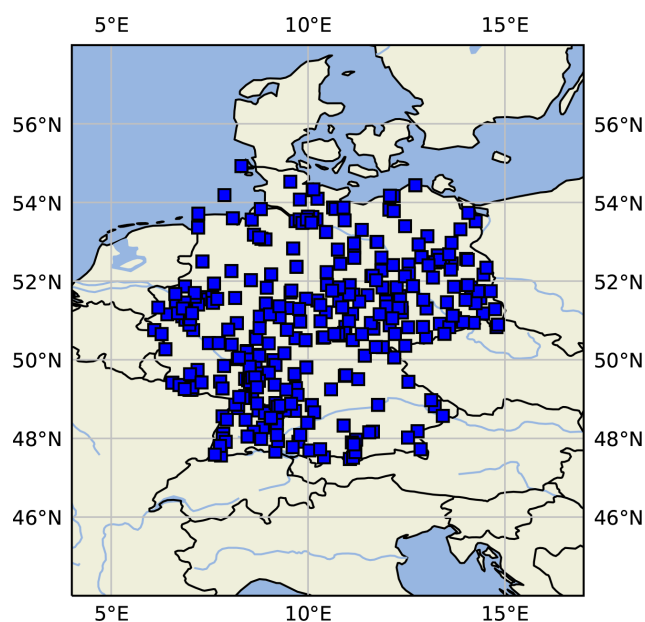


Figure 1. Map of central Europe showing the location of German measurement sites used in this study. This figure was created with Cartopy (Met Office, 2010–2015). Map data © OpenStreetMap contributors.

2.2 Data processing

We split the individual station time series into three non-overlapping time periods for training, validation, and testing which we will refer to as “set” from now on (see Fig. 2). We only used stations which at least have 1 year of valid data in one set. Firstly, the time span of the training dataset is ranging from 1 January 1997 to 31 December 2007. Secondly, the validation set is ranging from 1 January 2008 to 31 December 2009. Thirdly, the test set ranges from 1 January 2010 to 31 December 2015.

Due to changes in the measurement network over time, the number of stations in the three datasets differ: training

data comprise 312 stations, validation data 211 stations, and testing 203 stations. This is by far the largest air quality time series dataset that has been used in a machine learning study so far (see Table 1).

Supervised learning techniques require input data (\mathbf{X}) and a corresponding label (y) which we create for each station of the three sets as depicted in Algorithm 1.

Algorithm 1 Data preprocessing

- 1: Standardise time series to approximately mean zero and unit variance (approximation for z -transformation)
- 2: Linearly interpolate missing data (maximally one missing data point between valid samples)
- 3: **for all** Stations: Create samples (from standardised time series) **do**
- 4: Create inputs \mathbf{X} with variables of seven days ($-6d$) to ($0d$). Shape of \mathbf{X} : 7 by 1 by 9 (number of days, 1, number of variables)
- 5: Create labels y with ozone (dma8eu) concentrations for the next four days (1d to 4d). Shape of y : 1 by 4 (1, lead time)
- 6: **end for**
- 7: Remove all \mathbf{X} , y pairs which include any missing value
- 8: In the training set duplicate extremes (samples, where $y_i < -3$ or $y_i > 3$)
- 9: Permute samples in the training set (and only in the training set)
- 10: Create batches (collection of samples) of size 512

Samples within the same dataset (train, validation, and test) can overlap which means that one missing data point would appear up to seven times in the inputs \mathbf{X} and up to four times in the labels y . Consequently, one missing value will cause the removal of 11 samples (algorithm 1, line 7). As we want to keep the number of samples as high as possible, we decided to linearly interpolate (algorithm 1, line 2) the time series if only one consecutive value is missing. Table 4 shows the number of stations per dataset (train, val, test) and the corresponding amount of samples (pairs of inputs \mathbf{X} and labels y) per dataset. Moreover, Table A1 summarises all

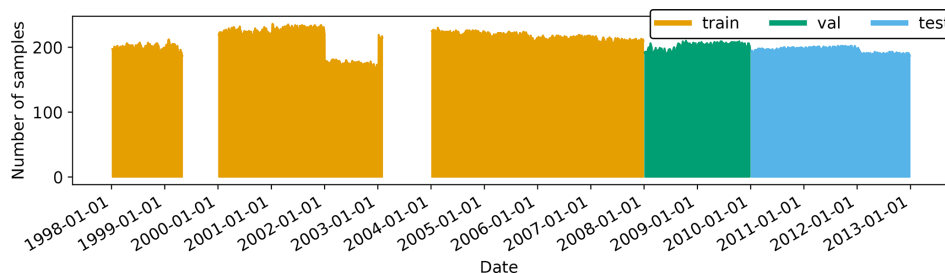


Figure 2. Data availability diagram combined for all variables and all stations. The training set is coloured in orange, the validation set in green, and the test set in blue. Gaps in 1999 and 2003 are caused by missing model data in the TOAR database.

samples per station individually. Figure 1 shows a map of all station locations.

We trained the neural network (details on the network architecture are given in Sect. 3) with data of the training set and tuned hyperparameters exclusively on the validation dataset. For the final analysis and model evaluation, we use the independent test dataset, which was neither used for training the models parameters, nor for tuning the hyperparameters. Random sampling, as is often done in other machine learning applications, and occasionally even in other air quality or weather applications of machine learning, would lead to overly optimistic results due to the multi-day auto-correlation of air quality and meteorological time series. Horowitz and Barakat (1979) already pointed to this issue when dealing with statistical tests. Likewise, the alternative split of the dataset into spatially segregated data could lead to the undesired effect that two or more neighbouring stations with high correlation between several paired variables fall into different datasets. Again, this would result in overly optimistic model results.

By applying a temporal split, we ensure that the training data do not directly influence the validation and test datasets. Therefore, the final results reflect the true generalisation capability of our forecasting model.

In accordance with other studies, our initial deep learning experiments with a subset of this data have shown that neural networks, just as other classical regression techniques, have a tendency to focus on the mean of the distribution and perform poorly on the extremes. However, especially the high concentration events are crucial in the air quality context due to their strong impact on human health and the adverse crop effects. Extreme values occur relatively seldomly in the dataset, and it is therefore difficult for the model to learn their associated patterns correctly. To increase the total number of values on the tails of the distribution during training, we append all samples where the standardised label (i.e. the normalised ozone concentration) is < -3 or > 3 for a second time on the training dataset (algorithm 1, line 8).

We selected a batch size of 512 samples (algorithm 1, line 10), because this size is a good compromise between minimising the loss function and optimising computing time per trained epoch. Experiments with larger and smaller batch

sizes did not yield significantly different results. Before creating the different training batches, we permute the ordering of samples per station in the training set to ensure that the distribution of each batch is similar to those of the full training dataset (algorithm 1, line 9). Otherwise, each batch would have an under-represented season and consequently would lead to undesired looping during training (e.g. no winter values in the first batch, no autumn values in the second batch).

3 Model setup

Our machine learning model is based on a convolutional layer neural network (LeCun et al., 1998), which was initially designed for pattern recognition in computer vision applications. It has been shown that such model architectures work equally well on time series data as other neural network architectures, which have been especially designed for this purpose, such as recurrent neural networks or LSTMs (Dauphin et al., 2017; Bai et al., 2018). Schmidhuber (2015) provides a historical review on different deep learning methods, while Ismail Fawaz et al. (2019) focus especially on deep neural networks for time series.

Our neural network named IntelliO3-ts, version 1.0, primarily consists of two inception blocks (Szegedy et al., 2015), which combine multiple convolutions, execute them in parallel, and concatenate all outputs in the last layer of each block. Figure A2 depicts one inception block including the first input layer, while Figs. A2 and A3 together show the entire model architecture including the final flat and output layers. We treat each input variable (see Table 2) as an individual channel (like R, G, B in images) and use time as the first dimension (this would correspond to the width axis of an image). Inputs (\mathbf{X}) consist of the variable values from 7 d (-6 to 0 d). Outputs are ozone concentration forecasts (dma8eu) for lead times up to 4 d (1 to 4 d). Therefore, we change the kernel sizes in the inception blocks from 1×1 , 3×3 , and 5×5 , as originally proposed by Szegedy et al. (2015), to 1×1 , 3×1 , and 5×1 . This allows the network to focus on different temporal relations. The 1×1 convolutions are also used for information compression (reduction of the number of filters) before larger convolutional kernels are applied (see

Table 4. Number of stations, total number of samples (pairs of \mathbf{X} and \mathbf{y}), and various statistics of number of samples per station in the training, validation, and test datasets. The number of stations per set varies as not all stations have data through the full period (see Table A1 for details).

	No. of stations	No. of samples	Mean	SD	Min	5 %	10 %	25 %	50 %	75 %	90 %	95 %	Max
Training	312	643 788	2063	802	369	668	939	1426	2191	2902	2989	3011	3045
Validation	211	145 030	687	61	370	532	625	690	710	721	721	721	721
Test	203	212 093	1044	92	466	759	983	1056	1075	1086	1086	1086	1086

Szegedy et al., 2015). This decreases the computational costs for training and evaluating the network. In order to conserve the initial input shape of the first dimension (time), we apply symmetric padding to minimise the introduction of artefacts related to the borders.

While the original proposed concept of inception blocks has one max-pooling tower alongside the different convolution stacks, we added a second pooling tower, which calculates the average on a kernel size of 3×1 . Thus, one inception block consists of three convolutional towers and two pooling (mean and max) towers. A tower is defined as a collection or stack of successive layers. The outputs of these towers are concatenated in the last layer of an inception block (see Fig. A2). Between individual inception blocks, we added dropout layers (Srivastava et al., 2014) with a dropout rate of 0.35 to improve the network's generalisation capability and prevent overfitting.

Moreover, we use batch normalisation layers (Ioffe and Szegedy, 2015) between each main convolution and activation layer to accelerate the training process (Fig. A2). Those normalisations ensure that for each batch the mean activation is zero with standard deviation of 1. As proposed in Szegedy et al. (2015), the network has an additional minor tail which helps to eliminate the vanishing gradient problem. Additionally, the minor tail helps to spread the internal representation of data as it strongly penalises large errors.

The loss function for the main tail is the mean squared error:

$$L_{\text{main}} = \frac{1}{n} \sum_i (y_{i,\text{true}} - y_{i,\text{pred}})^2, \quad (2)$$

while the loss function of the minor tail is

$$L_{\text{minor}} = \frac{1}{n} \sum_i (|y_{i,\text{true}} - y_{i,\text{pred}}|)^4. \quad (3)$$

All activation functions are exponential linear units (ELUs) (Clevert et al., 2016); only the final output activations are linear (minor and main tail).

The network is built with Keras 2.2.4 (Chollet, 2015) and uses TensorFlow 1.13.1 (Abadi et al., 2015) as the backend. We use Adam (Kingma and Ba, 2014) as optimiser and apply an initial learning rate of 10^{-4} (see also Sect. A5).

We train the model for 300 epochs on the Jülich Wizard for European Leadership Science (JUWELS; Jülich Supercomputing Centre, 2019) high-performance computing (HPC)

system which is operated by the Jülich Supercomputing Centre (see also Sect. A4 for further details regarding the software and hardware configurations).

4 Evaluation metrics and reference models

In general, one can interpret a supervised machine learning approach as an attempt to find an unknown function φ which maps an input pattern (\mathbf{X}) to the corresponding labels or the ground truth (\mathbf{y}). The machine learning model is consequently an estimator ($\hat{\varphi}$) which maps \mathbf{X} to an estimate $\hat{\mathbf{y}}$ of the ground truth. The goodness of the estimate is quantified by an error function, which the network tries to minimise during training. As the network is only an estimator of the true function, the mapping generally differs:

$$\varphi(\mathbf{X}) = \mathbf{y} \neq \hat{\mathbf{y}} = \hat{\varphi}(\mathbf{X}). \quad (4)$$

To evaluate the genuine added value of any meteorological or air quality forecasting model, it is essential to apply proper statistical metrics. The following section describes the verification tools, which are used in this study. We provide additional information on joint distributions as introduced by Murphy and Winkler (1987) in Sect. A2.

4.1 Scores and skill scores

To quantify a model's informational content, *scores* like the mean squared error (Eq. 5) are defined to provide an absolute performance measure, while *skill scores* provide a relative performance measure related to a reference forecast (Eq. 6).

$$\text{MSE}(\mathbf{m}, \mathbf{o}) = \frac{1}{N} \sum_{i=1}^N (m_i - o_i)^2 \geq 0 \quad (5)$$

Here, N is the number of forecast–observation pairs, \mathbf{m} is a vector containing all model forecasts, and \mathbf{o} is a vector containing the observations (Murphy, 1988).

A skill score S may be interpreted as the percentage of improvement of A over the reference A_{ref} . Its general form is

$$S = \frac{A - A_{\text{ref}}}{A_{\text{perf}} - A_{\text{ref}}}. \quad (6)$$

Here, A represents a general score, A_{ref} is the reference score, and A_{perf} the perfect score.

For $A = A_{\text{ref}}$, S becomes zero, indicating that the forecast of interest has no improvements over the reference forecast. A value of $S > 0$ indicates an improvement over the reference, while $S < 0$ indicates a deterioration. The informative value of a skill score strongly depends on the selected reference forecast. In the case of the mean squared error (Eq. 5), the perfect score is equal to zero and Eq. (6) reduces to

$$S(\mathbf{m}, \mathbf{r}, \mathbf{o}) = 1 - \frac{\text{MSE}(\mathbf{m}, \mathbf{o})}{\text{MSE}(\mathbf{r}, \mathbf{o})}, \quad (7)$$

where \mathbf{r} is a vector containing the reference forecast.

4.2 Reference models

We used three different reference models: persistence, climatology, and an ordinary least-square model (linear regression). For the climatological reference, we create four sub-reference models (see Sect. 4.2.2). In the following, we introduce our basic reference models.

4.2.1 Persistence model

One of the most straightforward models to build, which in general has good forecast skills on short lead times, is a persistence model. Today's observation of ozone dma8eu concentration is also the prediction for the next 4 d. Obviously, the skill of persistence decreases with increasing lead time. The good performance on short lead times is mainly due to the facts that weather conditions influencing ozone concentrations generally do not change rapidly, and that the chemical lifetime of ozone is long enough.

4.2.2 Climatological reference models

We create four different climatological reference models (Case I to Case IV), which are based on the climatology of observations by following Murphy (1988) (also with respect to their terminology, which means that the reference score A_{ref} is calculated by using the reference forecast \mathbf{r}).

The first reference forecast ($A_{\text{ref}} : \mathbf{r} = \bar{\mathbf{o}}$, Case I) is the internal single value climatology which is the mean of all observations during the test period. This unique value is then applied as reference for all forecasts. As this forecast has only one constant value which is the expectation value, this reference model is well calibrated but not refined at all.

The second reference ($A_{\text{ref}} : \mathbf{r} = \mathbf{o}^*$, Case II) is an internal multi-value climatology. Here, we calculate 12 arithmetic means, where each of the means is the monthly mean over all years in the test set (one mean for all Januaries from 2012 to 2015, one for all Februaries, etc.). The corresponding monthly mean is applied as reference. Therefore, Case II allows testing if the model has skill in reproducing the seasonal cycle of the observations.

The third reference ($A_{\text{ref}} : \mathbf{r} = \bar{\boldsymbol{\mu}}$, Case III) is an external single value climatology which is the mean of all available observations during the training and validation periods. This

reference does not include any direct information on the test set. Therefore, one can access the information if the forecast of interest captures features which are not directly present in the training and validation set.

Finally, the fourth reference ($A_{\text{ref}} : \mathbf{r} = \boldsymbol{\mu}^*$, Case IV) is an external multi-value climatology. A tabular summary explaining the individual formulae and terms following Murphy (1988) is given in Sect. A3. The last two references are calculated on a much longer time series than the first ones.

4.2.3 OLS reference model

The third reference model is an ordinary least-square (OLS) model. We train the OLS model by using the statsmodels package v0.10 (Seabold and Perktold, 2010). The OLS model is trained on the same data as the neural network (training set) and serves as a linear competitor.

5 Results

As described in Sect. 3, we split our data into three subsets (training, validation, and test set). We only used the independent test dataset to evaluate the forecasting capabilities of the IntelliO3-ts network. During training and hyperparameter optimisation, only the training and validation sets were used, respectively. Therefore, the following results reflect the true generalisation capability of IntelliO3-ts. Before discussing the results in detail below, we would like to point out again that this is the first time that one neural network has been trained to forecast data from an entire national air quality monitoring station network. Also, the network has been trained exclusively with time series data from air pollutant measurements and a meteorological reanalysis. No additional information, such as geographic coordinates, or other hints that could be used by the network to perform a station classification task, has been used. The impact of such extra information will be the subject of another study.

5.1 Forecasting results

Figure 3 shows the observed monthly O_3 -dma8eu distribution (green) and the corresponding network predictions for a lead time of up to 4 d (dark to light blue) summarised for all 203 stations in the test set. The network clearly captures the seasonal cycle. Nonetheless, the arithmetic mean (black triangles) and the median tend to shift towards their respective annual mean with increasing lead time (see also Fig. 6). In spring and autumn, the observed and forecasted distributions match well, while in summer and wintertime the network underestimates the interquartile range (IQR) and does not reproduce the extremes values (for example, the maxima in July/August or the minima in December/January/February).

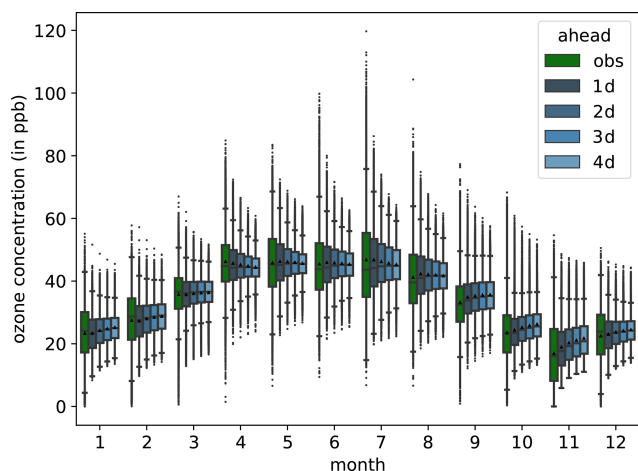


Figure 3. Monthly dma8eu ozone concentrations for all test stations as boxplots. Measurements are denoted by “obs” (green), while the forecasts are denoted by “1 d” (dark blue) to “4 d” (light blue). Whiskers have a maximal length of one interquartile range. The black triangles denote the arithmetic means.

5.2 Comparison with competitive models

The skill scores based on the mean squared error (MSE) evaluated over all stations in the test set are summarised in Fig. 4. In the left and centre groups of boxes and whiskers, the IntelliO3-ts model (labelled “CNN”) and the OLS model are compared against persistence as reference. The right group of boxes and whiskers shows the comparison between IntelliO3-ts and OLS. The mean skill score for IntelliO3-ts against persistence is positive and increases with time. The OLS forecast shows similar behaviour in terms of its temporal evolution but exhibits a slightly lower skill score throughout the 4 d forecasting period. The increases in skill score in both cases is mainly due to the decreasing performance of the persistence model (see also Sect. 4.2.1). Consequently, IntelliO3-ts shows a positive skill score when the OLS model is used as a reference, indicating a small genuine added value over the OLS model.

In comparison with climatological reference forecasts as introduced in Sect. 4.1 and summarised in Table A2, the skill scores are high for the first lead time (1 d) and decrease with increasing lead time (Fig. 5). Both cases with a single value as reference (internal Case I, external Case III) maintain a skill score above 0.4 over the 4 d. These high skill scores are a direct result of the fact that IntelliO3-ts captures the seasonal cycle as shown in Fig. 3, while the reference forecasts only report the overall mean as a single value prediction.

If the reference includes the seasonal variation (Case II and Case IV), the IntelliO3-ts skill score is still better than 0.4 for the first day (1 d), but then it decreases rapidly and even becomes negative on day 4 for Case II. The skill scores for Case II are lower than for Case IV as the reference climatology (i.e. the monthly mean values) is calculated on the

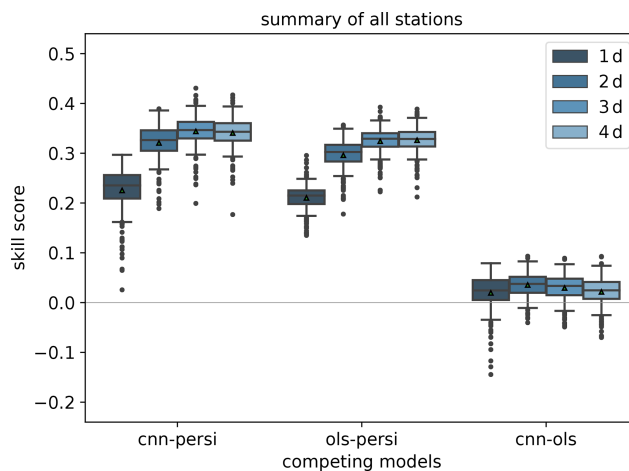


Figure 4. Skill scores of the IntelliO3-ts (cnn) versus the two reference models’ persistence (persi) and ordinary least square (ols) based on the mean squared error; separated for all lead times (1 d (dark blue) to 4 d (light blue)). Positive values denote that the first mentioned prediction model performs better than the reference model (mentioned as second). The triangles denote the arithmetic means.

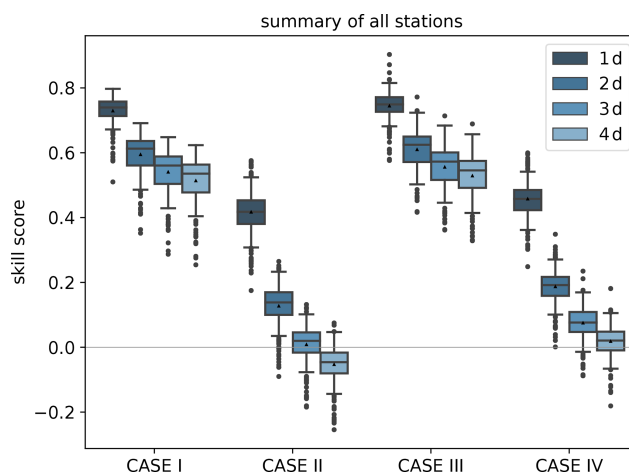


Figure 5. Skill scores of IntelliO3-ts with respect to climatological reference forecasts: with internal single value reference (Case I), internal multi-value (monthly) reference (Case II), external single (Case III), and external multi-value (monthly) reference (Case IV) for all lead times from 1 d (dark blue) to 4 d (light blue). Triangles denote the arithmetic means.

test set itself. These results show that, for the vast majority of stations, our model performs much better than a seasonal climatology for a 1 d forecast, and it is still substantially better than the climatology after 2 d. However, there are some stations which yield a negative skill score even on day 2 in the Case II comparison. Longer-term forecasts with this model setup do not add value compared to the computationally much cheaper monthly mean climatological forecast.

5.3 Analysis of joint distributions

The full joint distribution in terms of calibration refinement factorisation (Sect. A2) is shown in Fig. 6a (first lead time; 1 d) to d (last lead time; 4 d). The marginal distribution (refinement) is shown as histogram (light grey; sample size), while the conditional distribution (calibration) is presented by specific percentiles in different line styles. If the median (0.5th quantile, solid line) is below the reference, the network exhibits a high bias with respect to the observations, and vice versa. Obviously, quantiles in value regions with many data samples are more robust and therefore more credible than quantiles in data-sparse concentration regimes (Murphy et al., 1989). On the first lead time (d1; Fig. 6), the IntelliO3-ts network has a tendency to slightly overpredict concentrations $\lesssim 30$ ppb. On the other hand, the forecast underestimates concentrations above $\gtrsim 70$ ppb.

Both very high and very low forecasts are rare (note the logarithmic axis for the sample size). Therefore, the results in these regimes have to be treated with caution. Further detail is provided in Fig. A1, where the conditional biases are shown (terms BI, BII, and BIV in Sect. A3) which decrease the maximal climatological potential skill score (term AI; see also Table A2).

With increasing lead time, the model loses its capability to predict concentrations close to zero and high concentrations above 80 ppb. The marginal distribution develops a pronounced bimodal shape which is directly linked to the conditional biases. The number of high (extreme) ozone concentrations is relatively low, resulting in few training examples. The network tries to optimise the loss function with respect to the most common values. As a result, predictions of concentrations near the mean value of the distribution are generally more correct than predictions of values from the fringes of the distribution. Moreover, this also explains why the model does not perform substantially better than the monthly mean climatology forecasts (Case II, Case IV). This problem also becomes apparent in other studies. For example, Sayeed et al. (2020) focus their categorical analysis on a threshold value of 55 ppbv (maximum 8 h average) which corresponds to the air quality index value “moderate” (AQI 51 to 100), instead of the legal threshold value of 70 ppbv (U.S. Environmental Protection Agency, 2016, Table 5, therein), as the model shows better skills in this regime.

To shed more light on the factors influencing the forecast quality, we analyse the network performance individually for each season (DJF, MAM, JJA, and SON). Conditional quantile plots for individual seasons can be found in the Appendix (Sect. A6). As mentioned above, the bimodal shape of the marginal distribution is mainly caused by the network’s weakness to predict very high and low ozone concentrations. Moreover, the seasonal decomposition shows that the left mode is caused by the fall (SON) and winter (DJF) seasons (Figs. A7a–d and A4a–d). In both seasons, the most common values fall into the same concentration range, while the

right tail of SON is much more pronounced than for DJF, with higher values occurring primarily in September. In the summer season (JJA, Fig. A6a–d), the most frequently predicted values correspond to the location of the right mode of Fig. 6a–d. During DJF, MAM, and JJA, the model has a stronger tendency of under-forecasting with increasing lead time (median line moves above the reference line).

5.4 Relevance of input variables

To analyse the impact of individual input variables on the forecast results, we apply a bootstrapping technique as follows: we take the original input of one station, keep eight of the nine variables unaltered, and randomly draw (with replacement) the missing variable (20 times per variable per station). This destroys the temporal structure of this specific variable so that the network will no longer be able to use this information for forecasting. Compared to alternative approaches, such as re-training the model with fewer input variables, setting all variable values to zero, etc., this method has two main advantages: (i) the model does not need to be re-trained, and thus the evaluation occurs with the exact same weights that were learned from the full dataset, and (ii) the distribution of the input variable remains unchanged so that adverse effects, for example, due to correlated input variables, are excluded. However, we note that this method may underestimate the impact of a specific variable in the case of correlated input data, because in such cases the network will focus on the dominant feature (here ozone). Also, this analyses only evaluates the behaviour of the deep learning model and does not evaluate the impact of these variables on actual ozone formation in the atmosphere.

After the randomisation of one variable, we apply the trained model on this modified input data and compare the new prediction with the original one. For comparison, we apply the skill score (Eq. 6) based on the MSE where we use the original forecast as a reference. Consequently, the skill score will be negative if the bootstrapped variable has a significant impact on model performance. Figure 7 shows the skill scores for all variables (x axis) and lead times (dark (1 d) to light blue (4 d) boxplots). Ozone is the most crucial input variable, as it has by far the lowest skill score for all lead times. With increasing lead time, the skill score increases but stays lower than for any other variable. In contrast, the model does not derive much skill from the variables nitrogen oxide, nitrogen dioxide, and the planetary boundary layer height. In other words, the network does not perform worse, when randomly drawn values replace one of those original time series. Relative humidity, temperature, and the wind’s u component have an impact on the model performance. With increasing lead time, these influences decrease.

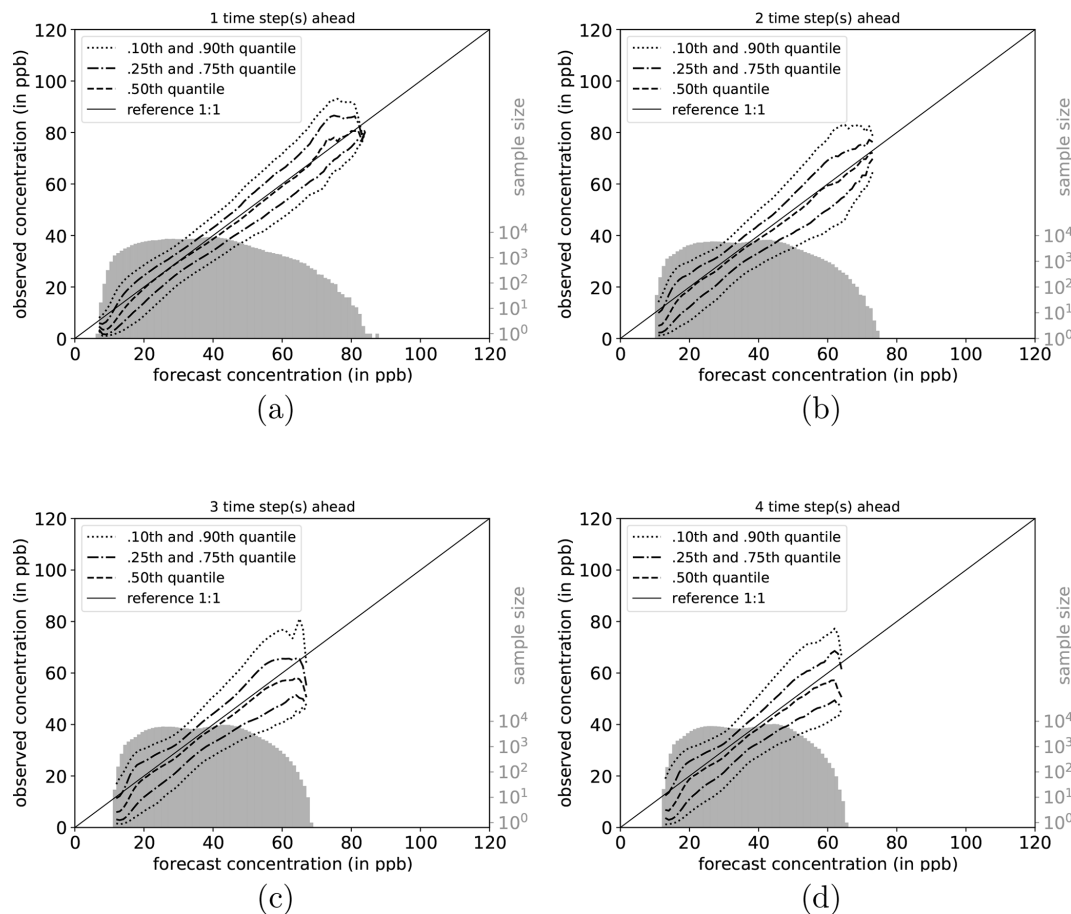


Figure 6. Conditional quantile plot for all IntelliO3-ts predictions for a lead time of 1 d (a), 2 d (b), 3 d (c), and 4 d (d). Conditional percentiles (0.10th and 0.90th, 0.25th and 0.75th and 0.50th) from the conditional distribution $f(o_j|m_i)$ are shown as lines in different styles. The reference line indicates a hypothetical perfect forecast. The marginal distribution of the forecast $f(m_i)$ is shown as log histogram (right axis, light grey). All calculations are done by using a bin size of 1 ppb. Quantiles are smoothed by using a rolling mean of a window size of 3. (After Murphy et al., 1989.)

6 Limitations and additional remarks

Even though IntelliO3-ts v1.0 generalises well on an unseen testing set (see Sect. 5), it still has some limitations related to the applied data split.

By splitting the data into three consecutive, non-overlapping sets, we ensure that the datasets are as independent as possible. On the other hand, this independence comes at the cost that changes of trends in the input variables may not be captured, especially as our input data are not detrended. Indeed, at European non-urban measurement sites, several ozone metrics related to high concentrations (e.g. fourth highest daily maximum 8 h (4MDA8) or the 95th percentile of hourly concentrations) show a significant decrease during our study period (1997 to 2015) (Fleming et al., 2018; Yan et al., 2018). Our data-splitting method for evaluating the generalisation capability is conservative in the sense that we evaluate the model on the test set, which has the largest possible distance to the training set. If our research model

shall be transformed into an operational system, we suggest applying online learning and use the latest available data for subsequent training cycles (see, for example, Sayeed et al., 2020).

7 Conclusions

In this study, we developed and evaluated IntelliO3-ts, a deep learning forecasting model for daily near-surface ozone concentrations (dma8eu) at arbitrary air quality monitoring stations in Germany. The model uses chemical (O_3 , NO, NO_2) and meteorological time series of the previous 6 d to create forecasts for up to 4 d into the future. IntelliO3-ts is based on convolutional inception blocks, which allow us to calculate concurrent convolutions with different kernel sizes. The model has been trained on 10 years of data from 312 background stations in Germany. Hyperparameter tuning and

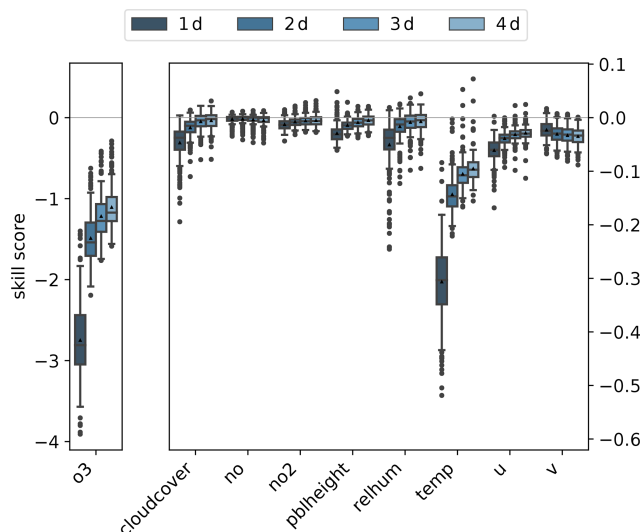


Figure 7. Skill scores of bootstrapped model predictions having the original forecast as the reference model are shown as boxplots for all lead times from 1 d (dark blue) to 4 d (light blue). The skill score for ozone is shown on the left y axis, while the skill score of the other variables is shown on the right y axis.

model evaluation were done with independent datasets of 2 and 6 years length, respectively.

The model generalises well and generates good quality forecasts for lead times up to 2 d. These forecasts are superior compared to the reference persistence, ordinary least squares, annual, and seasonal climatology models. After 2 d, the forecast quality degrades, and the forecast adds no value compared to a monthly mean climatology of dma8eu ozone levels. We could primarily attribute this to the network's tendency to converge to the mean monthly value. The model does not have any spatial context information which could counteract this tendency. Near-surface ozone concentrations at background stations are highly influenced by air mass advection, but the IntelliO3-ts network has no way of taking up-wind information into account yet. We will investigate spatial context approaches in a forthcoming study.

We observed that the model loses refinement with increasing lead time which results in unsatisfactory predictions on the tails of the observed ozone concentration. We were able to attribute this weakness to the under-representation of extreme (either very small or high) levels in the training dataset. This is a general problem for machine learning applications and regression methods. The machine learning community is investigating possible solutions to lessen the impact of such data imbalances, but their adaptation is beyond the scope of this paper as proposed techniques are not directly applicable to those time series (auto-correlation time).

Bootstrapping individual time series of the input data to analyse the importance of those variables on the predictive skill showed that the model mainly focused on the previous ozone concentrations. Temperature and relative humidity

only have a small effect on the model performance, while the time series of NO, NO₂, and planetary boundary layer (PBL) have no impact.

The IntelliO3-ts network extends previous work by using a new network architecture, and training one model on a much larger set of measurement station data and longer time periods. In light of Rasp and Lerch (2018), who used several neural networks to postprocess ensemble weather forecasts, we applied meteorological evaluation metrics to perform a point-by-point comparison, which is not common in the field of deep learning. We hope that the forecast quality of IntelliO3-ts can be further improved if we take spatial context information into account so that the advection of background ozone and ozone precursors can be learned by the model.

Appendix A

A1 Information on used stations

Table A1 lists all measurement stations which we used in this study. The table also shows the number of samples (\mathbf{X} , \mathbf{y}) for each of the three datasets (training, validation, and test).

Table A1. Number of samples (input and output pairs) per station separated by training, validation (val), and test dataset. “–” denotes no samples in a set.

	Training	Val	Test
Stat. ID			
DEBB001	1104	–	–
DEBB006	1455	–	–
DEBB007	–	721	1086
DEBB009	1438	–	–
DEBB021	2512	705	1052
DEBB024	2592	–	–
DEBB028	1353	–	–
DEBB031	2577	–	–
DEBB036	1008	–	–
DEBB038	1245	–	–
DEBB040	760	–	–
DEBB042	2902	721	1086
DEBB043	2194	–	–
DEBB048	2473	721	1075
DEBB050	2510	721	–
DEBB051	1006	–	–
DEBB053	2115	706	1086
DEBB055	1887	721	1053
DEBB063	1392	721	1086
DEBB064	1480	721	1086
DEBB065	1411	699	1086
DEBB066	1451	721	1086
DEBB067	1073	721	1086
DEBB075	–	721	1079
DEBB082	–	622	1086
DEBB083	–	–	1086
DEBE010	1372	707	1035
DEBE032	2441	690	1060
DEBE034	2506	671	1031
DEBE051	2433	694	1053
DEBE056	2481	678	1055
DEBE062	1941	677	1069
DEBW004	1440	721	1086
DEBW006	1451	721	1086
DEBW007	1440	699	–
DEBW008	656	–	–
DEBW010	3041	708	1086
DEBW013	1432	710	1079
DEBW019	2962	710	1078
DEBW020	1520	–	–

Table A1. Continued.

	Training	Val	Test
Stat. ID			
DEBW021	1579	–	–
DEBW023	1430	721	1078
DEBW024	3011	713	1086
DEBW025	1530	–	–
DEBW026	3005	721	–
DEBW027	3005	699	1075
DEBW028	1510	–	–
DEBW029	3012	721	1086
DEBW030	2966	–	–
DEBW031	2970	711	1069
DEBW032	2648	–	–
DEBW034	3045	707	–
DEBW035	2281	–	–
DEBW036	1183	–	–
DEBW037	3023	721	–
DEBW039	2999	710	1086
DEBW041	1581	–	–
DEBW042	2617	708	1067
DEBW044	1571	–	–
DEBW045	656	–	–
DEBW046	2990	699	1086
DEBW047	1563	–	–
DEBW049	646	–	–
DEBW050	1556	–	–
DEBW052	2652	721	1078
DEBW053	1574	–	–
DEBW054	1566	–	–
DEBW056	2938	721	1086
DEBW057	644	–	–
DEBW059	2974	721	1086
DEBW060	1571	–	–
DEBW065	1540	–	–
DEBW072	480	–	–
DEBW076	3035	721	708
DEBW081	2654	721	1079
DEBW084	1444	721	1042
DEBW087	3043	713	1086
DEBW094	2188	–	–
DEBW102	1122	–	–
DEBW103	2525	721	–
DEBW107	1801	714	1086
DEBW110	1107	721	–
DEBW111	1083	703	–
DEBW112	651	721	1079
DEBW113	678	–	–
DEBY002	2924	721	747
DEBY004	2917	707	1028
DEBY005	2959	714	1086
DEBY013	1412	652	980
DEBY017	1250	–	–

Table A1. Continued.

Stat. ID	Training	Val	Test
DEBY020	2976	721	1013
DEBY031	2927	678	1072
DEBY032	2975	721	711
DEBY034	1555	–	–
DEBY039	2554	721	1067
DEBY047	1895	721	754
DEBY049	2918	693	1066
DEBY052	2929	708	1035
DEBY062	1411	704	748
DEBY072	2907	690	1055
DEBY077	1409	721	724
DEBY079	2878	721	671
DEBY081	2932	523	713
DEBY082	1592	–	–
DEBY088	2986	713	1062
DEBY089	2644	721	1086
DEBY092	616	–	–
DEBY099	1828	703	725
DEBY109	1310	713	1071
DEBY113	1347	706	1086
DEBY118	937	705	727
DEBY122	–	–	877
DEHB001	2567	710	953
DEHB002	2287	702	1053
DEHB003	2546	695	–
DEHB004	1428	708	1037
DEHB005	2518	683	1066
DEHE001	1451	721	1086
DEHE008	2447	707	1075
DEHE010	1600	–	–
DEHE013	–	721	1086
DEHE017	1562	–	–
DEHE018	3016	721	1086
DEHE019	1958	–	–
DEHE022	2643	721	1086
DEHE023	2966	708	466
DEHE024	2935	710	1086
DEHE025	1554	–	–
DEHE026	2877	697	1086
DEHE027	1536	–	–
DEHE028	2946	710	1068
DEHE030	3028	721	1086
DEHE032	2926	714	1075
DEHE033	1835	–	–
DEHE034	1880	–	–
DEHE039	–	–	812
DEHE042	2966	721	1079
DEHE043	3004	721	1074
DEHE044	2543	721	1086
DEHE045	2535	699	1086
DEHE046	2513	714	1086

Table A1. Continued.

Stat. ID	Training	Val	Test
DEHE048	1043	–	–
DEHE050	1014	–	–
DEHE051	2331	721	1086
DEHE052	2078	713	1086
DEHE058	789	721	1086
DEHE060	704	672	1086
DEHH008	1439	721	1086
DEHH021	2624	710	1086
DEHH033	2148	682	1067
DEHH047	2175	696	1086
DEHH049	2150	721	1075
DEHH050	2131	721	1069
DEMV001	794	–	–
DEMV004	2908	721	1058
DEMV007	2986	721	1053
DEMV012	2885	710	1086
DEMV017	2507	708	1086
DEMV018	2113	710	–
DEMV019	1429	706	1086
DEMV021	600	688	1072
DEMV024	–	–	908
DENI011	2611	452	1086
DENI016	3034	627	1051
DENI019	2919	–	–
DENI020	2984	667	1086
DENI028	2927	516	1086
DENI029	2903	692	1086
DENI031	1410	451	1079
DENI038	2599	573	1083
DENI041	2935	525	1086
DENI042	2939	553	1072
DENI043	2941	606	1086
DENI051	2976	–	1072
DENI052	2910	529	1086
DENI054	2997	596	1086
DENI058	2398	–	1086
DENI059	2408	451	1079
DENI060	2386	677	1086
DENI062	2482	625	1080
DENI063	2385	460	1073
DENI077	–	–	1079
DENW004	1148	–	–
DENW006	1367	694	1026
DENW008	2511	701	1064
DENW010	1397	–	–
DENW013	1830	–	–
DENW015	1451	–	–
DENW018	1196	–	–
DENW028	1655	–	–
DENW029	2530	–	–
DENW030	2785	630	998

Table A1. Continued.

	Training	Val	Test
Stat. ID			
DENW036	1314	–	–
DENW038	2598	652	1079
DENW042	1185	–	–
DENW047	1350	–	–
DENW050	2488	–	–
DENW051	1206	–	–
DENW053	1795	678	1051
DENW059	1777	648	980
DENW062	1078	–	–
DENW063	2816	–	–
DENW064	2887	589	1052
DENW065	2877	550	1045
DENW066	2865	–	–
DENW067	2473	686	1079
DENW068	2892	447	1009
DENW071	1827	713	1071
DENW078	1382	681	1078
DENW079	2040	706	1086
DENW080	2147	689	1043
DENW081	2422	646	1058
DENW094	1980	627	1058
DENW095	1981	681	1071
DENW096	700	–	–
DENW179	766	699	1079
DENW247	–	572	1066
DERP001	1421	721	1068
DERP007	2652	721	1077
DERP013	2883	708	1067
DERP014	2967	703	1061
DERP015	2810	710	1047
DERP016	2962	721	1086
DERP017	2955	721	1055
DERP019	1413	708	1041
DERP021	2996	713	1025
DERP022	2989	701	1059
DERP025	2918	691	1086
DERP028	2802	678	1026
DESH005	962	–	–
DESH006	614	–	–
DESH008	3031	721	1053
DESH016	2635	698	–
DESH021	1107	–	–
DESH023	1700	721	1066
DESH033	–	721	1072
DESL003	1393	713	1086
DESL008	1371	–	–
DESL011	2776	710	1086
DESL012	–	–	1086

Table A1. Continued.

	Training	Val	Test
Stat. ID			
DESL017	2785	714	1086
DESL018	1656	710	1086
DESL019	1371	472	1057
DESN001	2925	689	1072
DESN004	3011	705	1086
DESN005	1166	–	–
DESN011	2613	694	1073
DESN012	2995	721	–
DESN014	2256	–	–
DESN017	3028	704	–
DESN019	2934	721	–
DESN024	3017	721	–
DESN028	401	–	–
DESN036	810	–	–
DESN045	2913	721	1064
DESN050	2939	710	–
DESN051	1451	685	1075
DESN057	1535	–	–
DESN059	2533	714	1078
DESN074	2534	702	1062
DESN076	2489	717	1075
DESN079	–	–	1071
DESN085	713	–	–
DESN092	–	536	1057
DEST002	3020	721	1075
DEST005	802	–	–
DEST011	2924	713	1075
DEST014	996	–	–
DEST022	805	–	–
DEST025	480	–	–
DEST028	2694	–	–
DEST030	2282	–	–
DEST031	796	–	–
DEST032	447	–	–
DEST039	2971	676	1069
DEST044	2923	709	1086
DEST050	2672	706	1075
DEST052	1484	–	–
DEST061	814	–	–
DEST063	1241	–	–
DEST066	2991	659	1086
DEST069	2589	707	–
DEST070	1488	–	–
DEST071	462	–	–
DEST072	2641	703	–
DEST077	1611	663	1086
DEST078	3042	709	–
DEST089	2467	710	1048
DEST098	1422	649	1086

Table A1. Continued.

	Training	Val	Test
Stat. ID			
DEST104	–	–	1061
DETH005	3030	721	1075
DETH009	2995	721	1086
DETH013	2945	710	1086
DETH016	1937	–	–
DETH018	3027	721	1086
DETH020	3002	721	1086
DETH024	1193	–	–
DETH025	2542	370	–
DETH026	1474	721	1072
DETH027	1444	705	1086
DETH036	2996	721	1086
DETH040	2926	721	1078
DETH041	3003	710	1043
DETH042	2993	697	1086
DETH060	2519	721	1086
DETH061	2465	721	1063
DETH095	–	–	1059
DETH096	–	–	898
DEUB001	1202	721	1075
DEUB003	1436	–	–
DEUB004	2746	721	932
DEUB005	1422	721	974
DEUB013	414	–	–
DEUB021	369	–	–
DEUB026	1768	–	–
DEUB028	2602	603	1086
DEUB029	2834	721	1062
DEUB030	2893	710	947
DEUB031	1845	–	–
DEUB032	1629	–	–
DEUB033	2034	–	–
DEUB034	1434	–	–
DEUB035	1977	–	–
DEUB036	411	–	–
DEUB038	1628	–	–
DEUB039	1676	–	–
DEUB040	1549	–	–
DEUB041	781	–	–
DEUB042	687	–	–
Total stations	312	211	203
Total samples	643 788	145 030	212 093

A2 Joint distributions

Forecasts and observations are treated as random variables. Let $p(m, o)$ represent the joint distribution of a model's forecast m and an observation o , which contains information on the forecast, the observation, and the relationship between both of them (Murphy and Winkler, 1987). To access specific pieces of information, we factorise the joint distribution into a conditional and a marginal distribution in two ways. The first factorisation is called calibration refinement and reads

$$p(m, o) = p(o|m) p(m), \quad (\text{A1})$$

where $p(o|m)$ is the conditional distribution of observing o given the forecast m , and $p(m)$ is the marginal distribution which indicates how often different forecast values are used (Murphy and Winkler, 1987; Wilks, 2006). A continuous forecast is perfectly calibrated if

$$E(o|m) = m \quad (\text{A2})$$

holds, where $E(o|m)$ is the expected value of o given the forecast m . The marginal distribution $p(m)$ is a measure of how often different forecasts are made and is therefore also called refinement or sharpness. Both distributions are important to evaluate a model's performance. Murphy and Winkler (1987) pointed out that a perfectly calibrated forecast is worth nothing if it lacks refinement.

The second factorisation is called the likelihood-base rate and consequently is given by

$$p(m, o) = p(m|o) p(o), \quad (\text{A3})$$

where $p(m|o)$ is the conditional distribution of forecast m given that o was observed. $p(o)$ is the marginal distribution which only contains information about the underlying rate of occurrence of observed values and is therefore also called the sample climatological distribution (Wilks, 2006).

A3 Mean squared error decomposition (Murphy, 1988)

This section provides additional information about the MSE decomposition introduced by Murphy (1988). The MSE decomposition is performed as

$$\text{MSE}(\mathbf{m}, \mathbf{o}) = \frac{1}{n} \sum_{i=1}^n ((m_i - \bar{m}) - (o_i - \bar{o}) + (\bar{m} - \bar{o}))^2 \quad (\text{A4})$$

$$= (\bar{m} - \bar{o})^2 + \sigma_m^2 + \sigma_o^2 - 2\sigma_{mo} \quad (\text{A5})$$

$$= (\bar{m} - \bar{o})^2 + \sigma_m^2 + \sigma_o^2 - 2\sigma_m \sigma_o \rho_{mo}. \quad (\text{A6})$$

Here, σ_m (σ_o) is the sample variance of the forecasts (observations) and σ_{mo} is the sample covariance of the forecasts and observations, which is given by $\sigma_{mo} = \frac{1}{n} \sum_{i=1}^n (m_i - \bar{m})(o_i - \bar{o})$. ρ_{mo} is the sample coefficient of

correlation between forecast and observation.

Case I:

$$S(m, \bar{o}, o) = \underbrace{\rho_{mo}^2}_{\text{AI}} - \underbrace{\left(\rho_{mo} - \frac{\sigma_m}{\sigma_o}\right)^2}_{\text{BI}} - \underbrace{\left(\frac{\bar{m} - \bar{o}}{\sigma_o}\right)^2}_{\text{CI}} \quad (\text{A7})$$

Case II:

$$S(m, o^*, o) = \frac{\text{AI} - \text{BI} - \text{CI} - \rho_{o^*o}^2 + \left(\rho_{o^*o} - \frac{\sigma_{o^*}}{\sigma_o}\right)^2}{1 - \underbrace{\rho_{o^*o}^2}_{\text{AII}} + \underbrace{\left(\rho_{o^*o} - \frac{\sigma_{o^*}}{\sigma_o}\right)^2}_{\text{BII}}} \quad (\text{A8})$$

Case III:

$$S(m, \bar{\mu}, o) = \frac{\text{AI} - \text{BI} - \text{CI} + \left(\frac{\bar{\mu} - \bar{o}}{\sigma_o}\right)^2}{1 + \underbrace{\left(\frac{\bar{\mu} - \bar{o}}{\sigma_o}\right)^2}_{\text{AIII}}} \quad (\text{A9})$$

Case IV:

$$S(m, \mu, o) = \frac{\text{AI} - \text{BI} - \text{CI} - \rho_{\mu o}^2 + \left(\rho_{\mu o} - \frac{\sigma_{\mu}}{\sigma_o}\right)^2 + \left(\frac{\bar{\mu} - \bar{o}}{\sigma_o}\right)^2}{1 - \underbrace{\rho_{\mu o}^2}_{\text{AIV}} + \underbrace{\left(\rho_{\mu o} - \frac{\sigma_{\mu}}{\sigma_o}\right)^2}_{\text{BIV}} + \underbrace{\left(\frac{\bar{\mu} - \bar{o}}{\sigma_o}\right)^2}_{\text{CIV}}} \quad (\text{A10})$$

The term AI is the square of the sample correlation coefficient and might be interpreted as the strength of linear relationship between the forecast and the observation. This term ranges from 0 (no correlation) to 1 (perfect correlation). The term BI includes the square of the differences between the sample correlation coefficient and the ratio of standard deviation of the forecast and observation. Therefore, BI is a measure of the conditional bias of the forecast which is always positive due to the square and tends to decrease skill as it is a subtrahend. The last term, which is included in all cases (I–IV), is CI and contains the square of the difference of the mean forecast and mean observation divided by the variance of the observation. Therefore, CI is a measure of the unconditional bias in the forecast and, again, tends to decrease the skill as it is a subtrahend which is always greater than or equal to zero.

In the case of multi-value internal climatology (Case II, Eq. A8), two additional terms appear in the dominator as

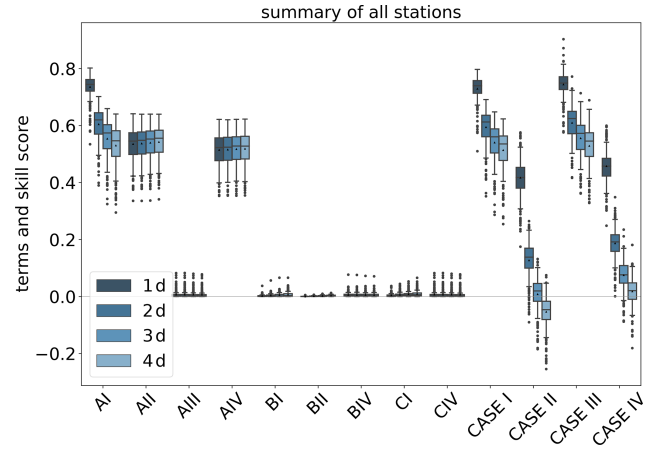


Figure A1. Skill scores of IntelliO3-ts with respect to climatological reference forecast, with internal single value reference (Case I), internal multi-value (monthly) reference (Case II), external single (Case III), and external multi-value (monthly) reference (Case IV) for all lead times from 1 d (dark blue) to 4 d (light blue). All terms are described in Sect. A3. Triangles denote the arithmetic means.

well as the numerator which tend to decrease skill in general and only vanish if $2\rho_{o^*o} = \sigma_{\mu}/\sigma_o$. In Case III, the additional term AIII appears that includes the square of the difference between the mean external and the internal climatology divided by the variance of the observation. AIII leads to an increase of skill for any difference in the means of external and internal climatologies.

Three additional terms (AIV, BIV, and CIV) appear if Eq. (7) is decomposed by using a multi-value external climatology as reference forecast (Case IV). These terms only vanish if $2\rho_{\mu o} = \sigma_{\mu}/\sigma_o$ and $\bar{\mu} = \bar{o}$. A summary of all four cases and all terms included is given in Table A2.

Figure A1 also includes all individual terms as described above.

A4 Additional information on JUWELS

Each node on JUWELS (Jülich Supercomputing Centre, 2019) which is part of the graphical processor unit (GPU) partition is equipped with four NVIDIA Volta V100 GPUs. The user guide for JUWELS is available from <https://apps.fz-juelich.de/jsc/hps/juwels/index.html> (last access: 12 November 2020).

A5 Detailed model settings

Figures A2 and A3 show the full architecture of IntelliO3-ts including all individual layers and tails. Table A3 lists the specific compile options per keyword of Keras' compile method. Table A4 summarises additional settings for the specific architecture.

Table A2. Summarised skill scores $S(m, r, o)$ based on the MSE (Cases I–IV) and relating terms (AI–CIV) as described in Sect. A3. m denotes the prediction model, r is the reference, and o denotes the observation. The “ \times ” sign marks if a term (AI to CIV) appears in the different factorisations. The following abbreviations are used: corr. for correlation, obs. for observation, ref. reference (forecast), cond. for conditional, int. for internal, and ext. for external.

Term	Case I	Case II	Case III	Case IV	Formula	Meaning
r :	\bar{o} int. single	o^* int. multi	$\bar{\mu}$ ext. single	μ ext. multi		reference
AI	\times	\times	\times	\times	ρ_{mo}^2	potential skill
AII		\times			$\rho_{o^*o}^2$	corr. obs.–ref.
AIII			\times		$\left(\frac{\bar{\mu}-\bar{o}}{\sigma_o}\right)^2$	trend
AIV				\times	$\rho_{\mu o}^2$	corr. obs.–ref.
BI	\times	\times	\times	\times	$\left(\rho_{mo} - \frac{\sigma_m}{\sigma_o}\right)^2$	cond. bias
BII		\times			$\left(\rho_{o^*o} - \frac{\sigma_{o^*}}{\sigma_o}\right)^2$	cond. bias
BIV				\times	$\left(\rho_{\mu o}^2 - \frac{\sigma_\mu}{\sigma_o}\right)^2$	cond. bias
CI	\times	\times	\times	\times	$\left(\frac{\bar{m}-\bar{o}}{\sigma_o}\right)^2$	uncond. bias
CIV				\times	$\left(\frac{\bar{\mu}-\bar{o}}{\sigma_o}\right)^2$	trend
Equation	(A7)	(A8)	(A9)	(A10)		

Table A3. Specific compile options passed to Keras’ compile method. Other keywords which are not listed in this table are left with default values.

Keyword	Value
optimizer	adam(lr=0.001, amsgrad=True)
loss	Eqs. (3), (2)
loss_weight	0.01, 0.99

Table A4. Specific information and rates used to set up the model architecture.

Setting	Value
Dropout rate	0.35
Regularizer	keras.regularizers.l2(0.01)
Epochs	300
Activation (all without last layer)	ELU
Activation (output layers)	linear
Padding	symmetric padding

A6 Seasonal decomposition of conditional quantiles

The following section contains all conditional quantile plots decomposed for all seasons (DJF: Fig. A4a–d, MAM: Fig. A5a–d, JJA: Fig. A6a–d, and SON: Fig. A7a–d).

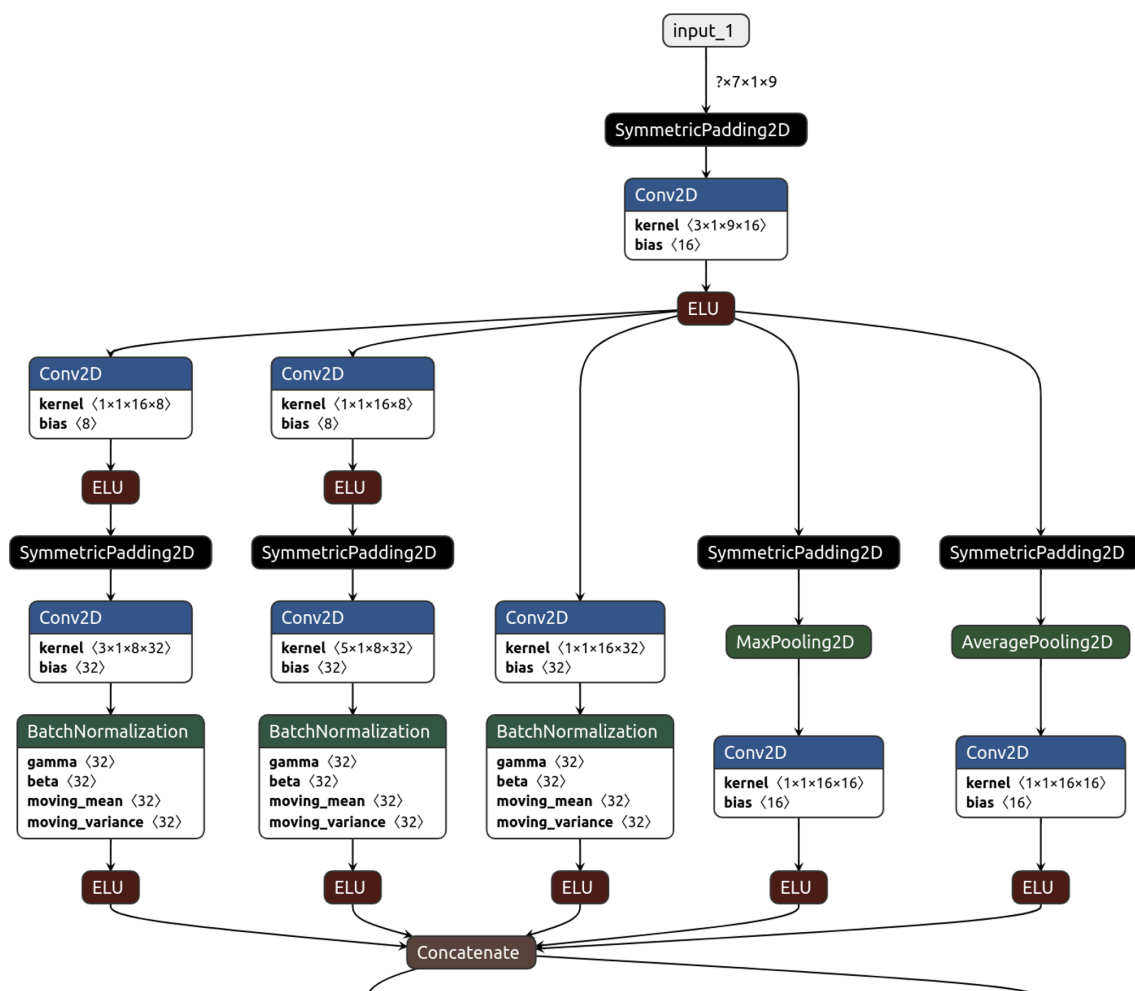


Figure A2. First part of the network showing the input, the first padding, convolution and activation, and the first inception block. This figure was created with Netron (Roeder, 2020).

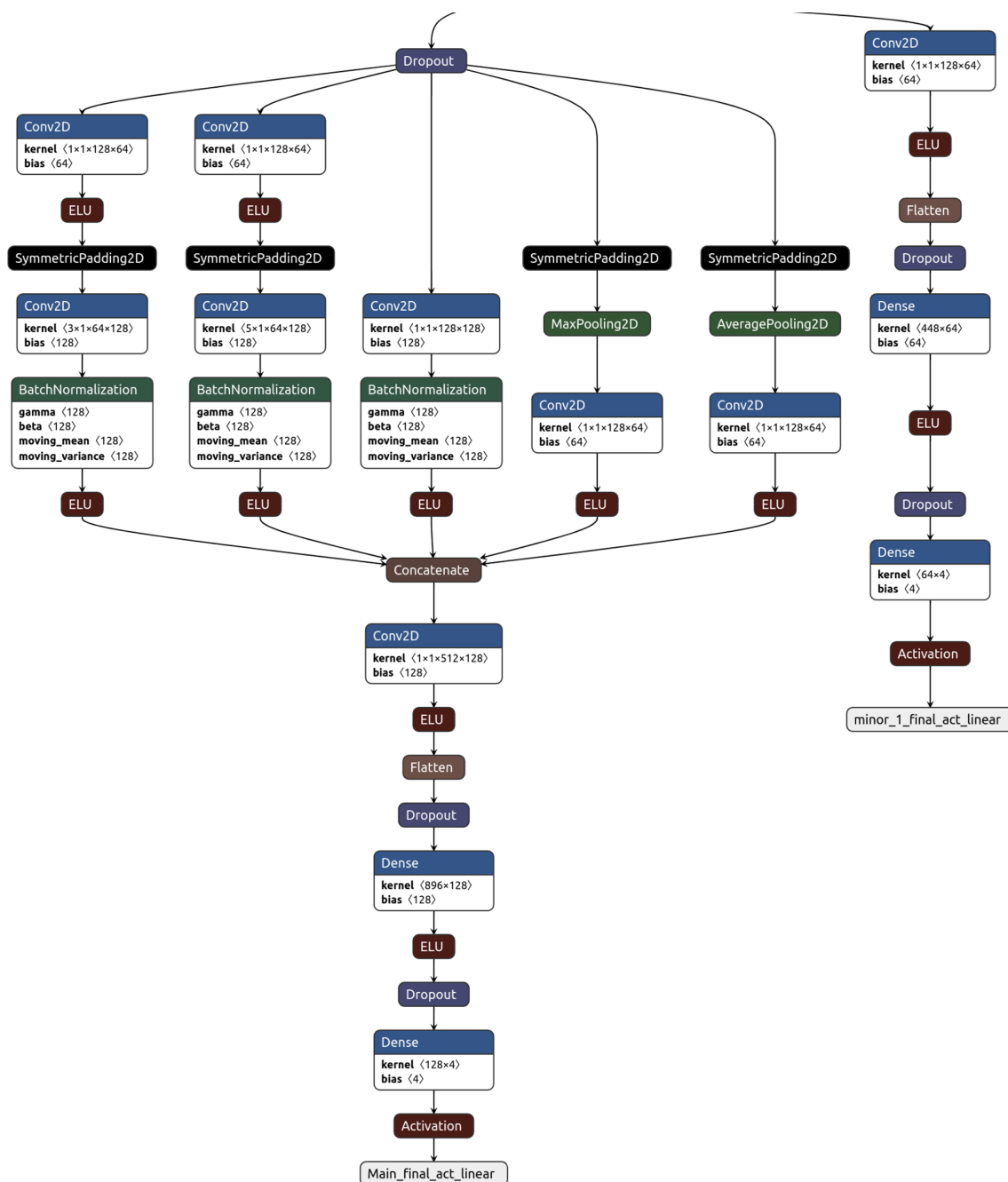


Figure A3. Second part of the network after the “concatenate” layer in Fig. A2, showing the minor output branch, the second inception block, and the main output branch. This figure was created with Netron (Roeder, 2020).

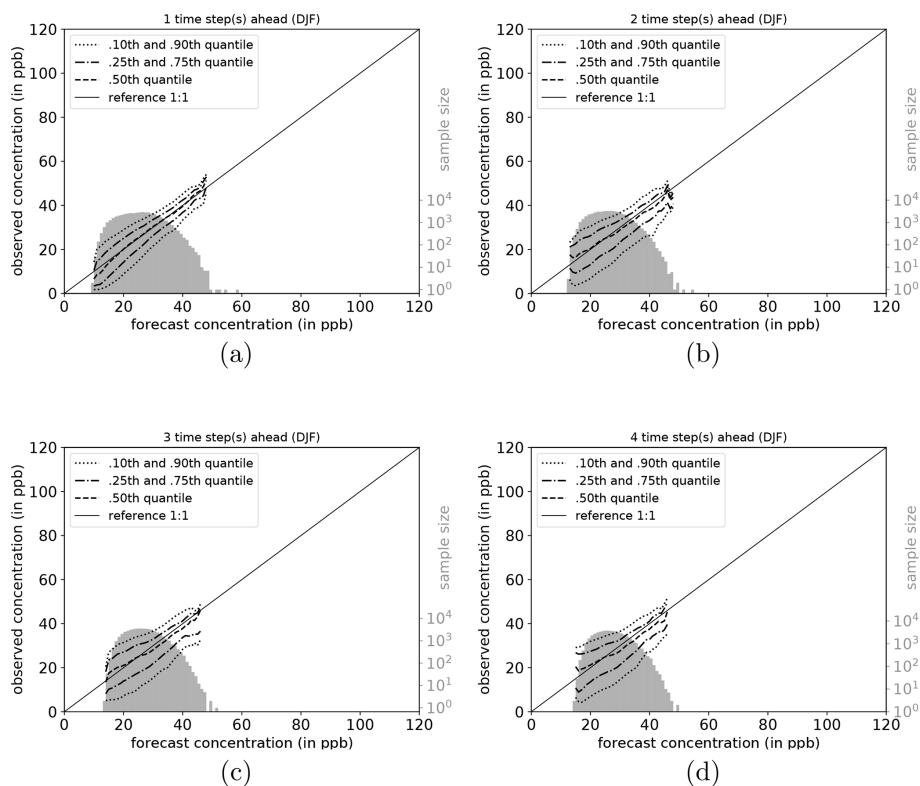


Figure A4. Same as Fig. 6 but for DJF.

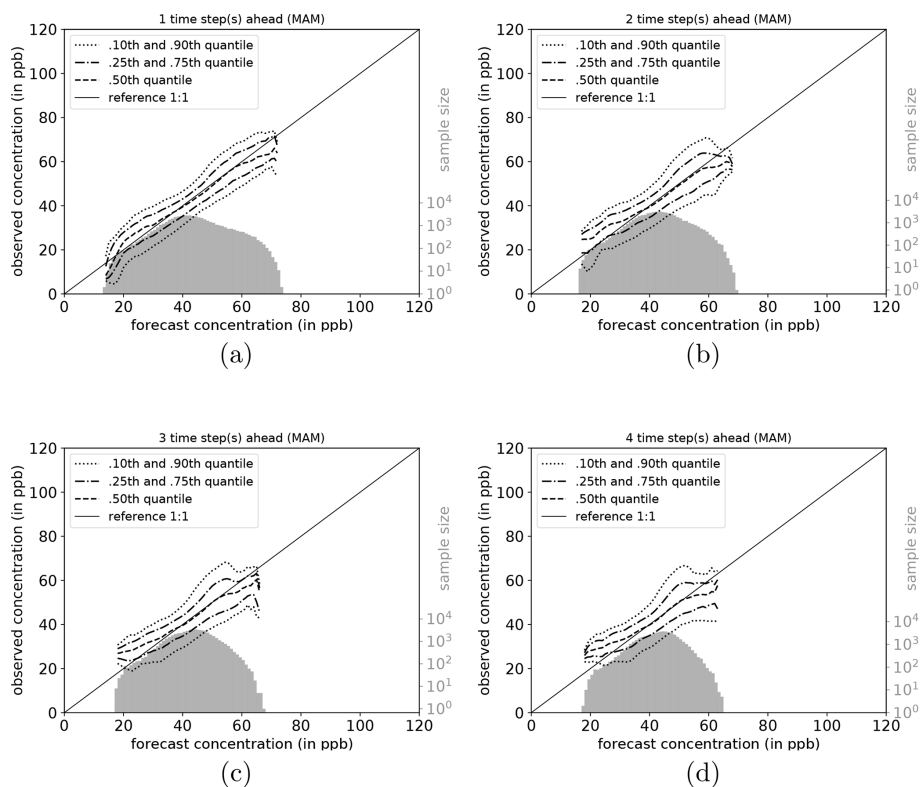


Figure A5. Same as Fig. 6 but for MAM.

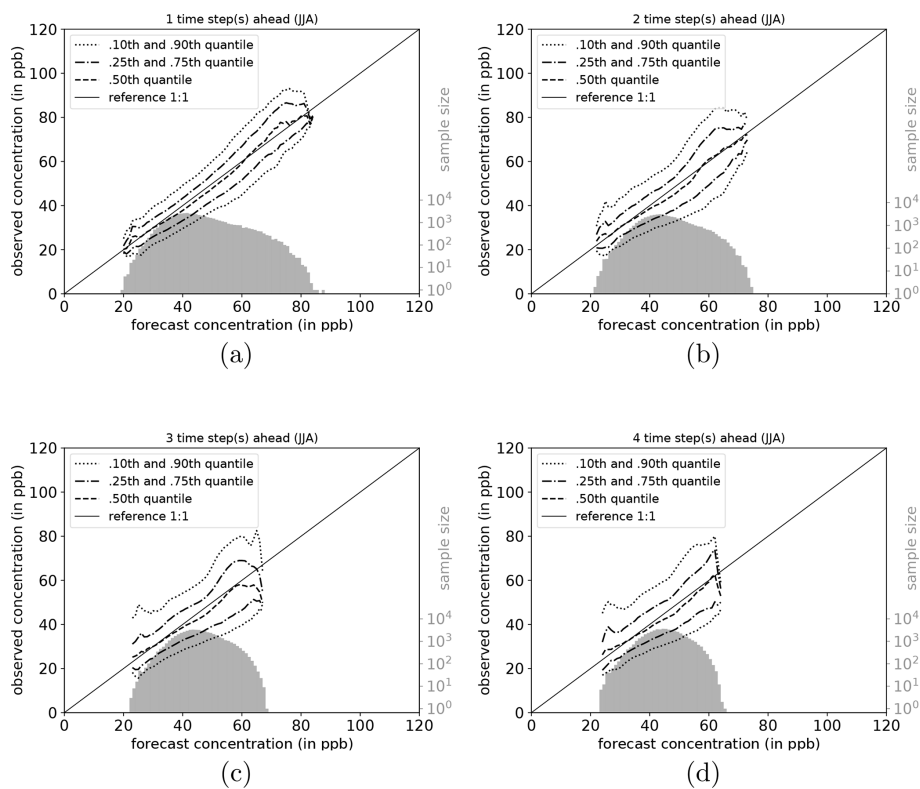


Figure A6. Same as Fig. 6 but for JJA.

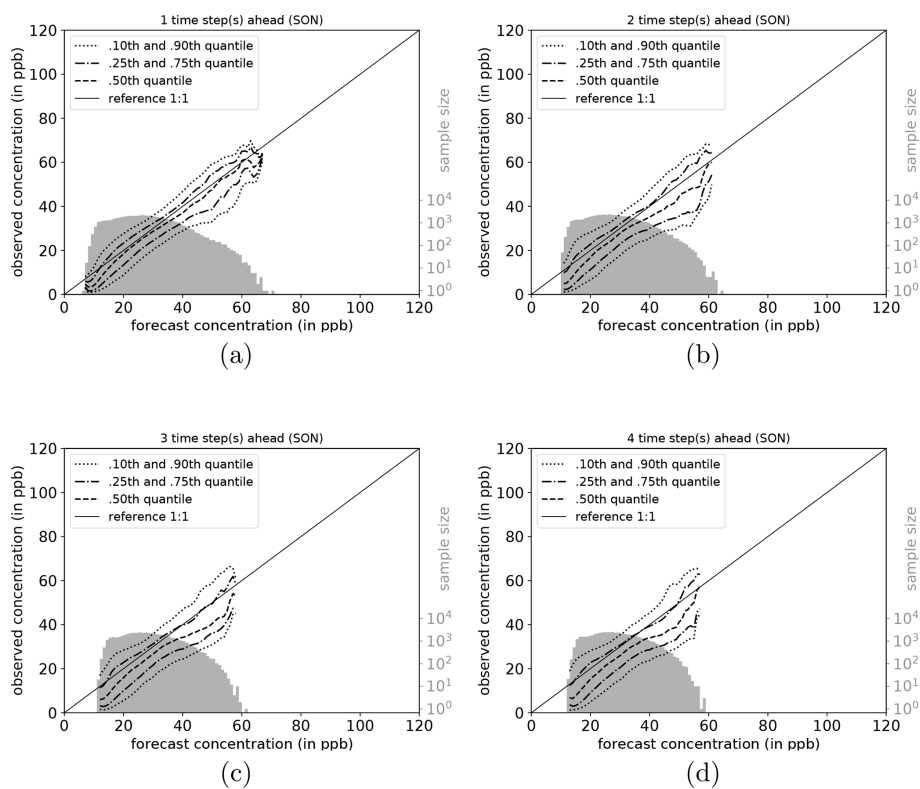


Figure A7. Same as Fig. 6 but for SON.

Code and data availability. The current version of IntelliO3-ts is available from the project website: <https://gitlab.version.fz-juelich.de/toar/mlair/-/tree/IntelliO3-ts> (last access: 12 November 2020) under the MIT licence (<http://opensource.org/licenses/mit-license.php>, last access: 18 December 2020). The exact versions of the model and data used to produce the results in this paper are archived on b2share at <https://doi.org/10.23728/b2share.5042cda41a4c49769cc4010d231ecdec> (Kleinert et al., 2020b). The initial version which was used for the initial submission is also archived on b2share at <https://doi.org/10.34730/c5dae21fac954aa6bdb4e86172221526> (Kleinert et al., 2020a).

Author contributions. FK and MGS developed the concept of the study. All authors jointly developed the concept of the machine learning model. FK implemented the neural network and performed the experiment. FK had the lead in writing the manuscript with contributions from LHL and MGS. LHL had the technical lead in code development and workflow design. All authors revised the final manuscript and submitted it to *GMD*.

Competing interests. The authors declare that they have no conflict of interest.

Acknowledgements. We are thankful to all air quality data providers which made their data available in the TOAR database. Moreover, we thank the meteorological section of the Institute of Geosciences at the University of Bonn, which provided the COSMO reanalysis data. We thank Sabine Schröder for the help in accessing data through the JOIN interface and Jenia Jitsev for helpful discussions.

The authors gratefully acknowledge the Gauss Centre for Supercomputing e.V. (<http://www.gauss-centre.eu>, last access: 18 December 2020) for funding this project by providing computing time through the John von Neumann Institute for Computing (NIC) on the GCS Supercomputer JUWELS at Jülich Supercomputing Centre (JSC). We are grateful to the anonymous reviewers for the constructive review and encouraging comments.

Financial support. This research has been supported by the European Research Council (grant no. IntelliAQ (787576)).

The article processing charges for this open-access publication were covered by a Research Centre of the Helmholtz Association.

Review statement. This paper was edited by Juan Antonio Añel and reviewed by two anonymous referees.

References

Abadi, M., Agarwal, A., Barham, P., Brevdo, E., Chen, Z., Citro, C., Corrado, G. S., Davis, A., Dean, J., Devin, M., Ghemawat, S.,

Goodfellow, I., Harp, A., Irving, G., Isard, M., Jia, Y., Jozefowicz, R., Kaiser, M., Kudlur, M., Levenberg, J., Mané, M., Monga, R., Moore, S., Murray, D., Olah, C., Schuster, M., Shlens, J., Steiner, J., Sutskever, I., Talwar, J., Tucker, P., Vanhoucke, V., Vasudevan, V., Viégas, F., Vinyals, O., Warden, P., Wattenberg M., Wicke, M., Yu, Y., and Zheng, X.: TensorFlow: Large-Scale Machine Learning on Heterogeneous Systems, available at: <https://www.tensorflow.org/> (last access: 18 December 2020), 2015.

Abdul Aziz, F. A. B., Abd. Rahman, N., and Mohd Ali, J.: Tropospheric Ozone Formation Estimation in Urban City, Bangi, Using Artificial Neural Network (ANN), *Comput. Intel. Neurosci.*, 2019, 1–10, <https://doi.org/10.1155/2019/6252983>, 2019.

Abdul-Wahab, S. A., Bakheit, C. S., and Al-Alawi, S. M.: Principal component and multiple regression analysis in modelling of ground-level ozone and factors affecting its concentrations, *Environ. Modell. Softw.*, 20, 1263–1271, <https://doi.org/10.1016/j.envsoft.2004.09.001>, 2005.

Avnery, S., Mauzerall, D. L., Liu, J., and Horowitz, L. W.: Global crop yield reductions due to surface ozone exposure: 1. Year 2000 crop production losses and economic damage, *Atmos. Environ.*, 45, 2284–2296, <https://doi.org/10.1016/j.atmosenv.2010.11.045>, 2011.

Bai, S., Kolter, J. Z., and Koltun, V.: An Empirical Evaluation of Generic Convolutional and Recurrent Networks for Sequence Modeling, *arXiv [preprint]*, arXiv:1803.01271, 2018.

Bell, M. L., Zanobetti, A., and Dominici, F.: Who is More Affected by Ozone Pollution? A Systematic Review and Meta-Analysis, *Am. J. Epidemiol.*, 180, 15–28, <https://doi.org/10.1093/aje/kwu115>, 2014.

Bollmeyer, C., Keller, J. D., Ohlwein, C., Wahl, S., Crewell, S., Friederichs, P., Hense, A., Keune, J., Kneifel, S., Pscheidt, I., Redl, S., and Steinke, S.: Towards a high-resolution regional re-analysis for the European CORDEX domain, *Q. J. Roy. Meteor. Soc.*, 141, 1–15, <https://doi.org/10.1002/qj.2486>, 2015.

Brunner, D., Savage, N., Jorba, O., Eder, B., Giordano, L., Badia, A., Balzarini, A., Baró, R., Bianconi, R., Chemel, C., Curci, G., Forkel, R., Jiménez-Guerrero, P., Hirtl, M., Hodzic, A., Honzak, L., Im, U., Knote, C., Makar, P., Manders-Groot, A., van Meijgaard, E., Neal, L., Pérez, J. L., Pirovano, G., San Jose, R., Schröder, W., Sokhi, R. S., Syrakov, D., Torian, A., Tuccella, P., Werhahn, J., Wolke, R., Yahya, K., Zabkar, R., Zhang, Y., Hogrefe, C., and Galmarini, S.: Comparative analysis of meteorological performance of coupled chemistry-meteorology models in the context of AQMEII phase 2, *Atmos. Environ.*, 115, 470–498, <https://doi.org/10.1016/j.atmosenv.2014.12.032>, 2015.

Chollet, F.: Keras, available at: <https://keras.io> (last access: 18 December 2020), 2015.

Clevert, D.-A., Unterthiner, T., and Hochreiter, S.: Fast and Accurate Deep Network Learning by Exponential Linear Units (ELUs), *arXiv [preprint]*, arXiv:1511.07289, 2016.

Cobourn, W. G., Dolcine, L., French, M., and Hubbard, M. C.: A Comparison of Nonlinear Regression and Neural Network Models for Ground-Level Ozone Forecasting, *J. Air Waste Ma.*, 50, 1999–2009, <https://doi.org/10.1080/10473289.2000.10464228>, 2000.

Collins, W. J., Stevenson, D. S., Johnson, C. E., and Derwent, R. G.: Tropospheric Ozone in a Global-Scale Three-Dimensional Lagrangian Model and Its Response to

- NOX Emission Controls, *J. Atmos. Chem.*, 26, 223–274, <https://doi.org/10.1023/A:1005836531979>, 1997.
- Comrie, A. C.: Comparing Neural Networks and Regression Models for Ozone Forecasting, *J. Air Waste Ma.*, 47, 653–663, <https://doi.org/10.1080/10473289.1997.10463925>, 1997.
- Dauphin, Y. N., Fan, A., Auli, M., and Grangier, D.: Language Modeling with Gated Convolutional Networks, *arXiv [preprint]*, *arXiv:1612.08083*, 2017.
- Donner, L. J., Wyman, B. L., Hemler, R. S., Horowitz, L. W., Ming, Y., Zhao, M., Golaz, J.-C., Ginoux, P., Lin, S.-J., Schwarzkopf, M. D., Austin, J., Alaka, G., Cooke, W. F., Delworth, T. L., Freidenreich, S. M., Gordon, C. T., Griffies, S. M., Held, I. M., Hurlin, W. J., Klein, S. A., Knutson, T. R., Langenhorst, A. R., Lee, H.-C., Lin, Y., Magi, B. I., Malyshev, S. L., Milly, P. C. D., Naik, V., Nath, M. J., Pincus, R., Ploshay, J. J., Ramaswamy, V., Seman, C. J., Shevliakova, E., Sirutis, J. J., Stern, W. F., Stouffer, R. J., Wilson, R. J., Winton, M., Wittenberg, A. T., and Zeng, F.: The Dynamical Core, Physical Parameterizations, and Basic Simulation Characteristics of the Atmospheric Component AM3 of the GFDL Global Coupled Model CM3, *J. Climate*, 24, 3484–3519, <https://doi.org/10.1175/2011JCLI3955.1>, 2011.
- Dye, T. S.: Guidelines for developing an air quality (ozone and PM_{2.5}) forecasting program, US Environmental Protection Agency, Office of Air Quality Planning and Standards, Information Transfer and Program Integration Division, AIRNow Program, available at: <https://nepis.epa.gov/Exe/ZyPURL.cgi?Dockey=2000F0ZT.txt> (last access: 18 December 2020), 2003.
- Eslami, E., Choi, Y., Lops, Y., and Sayeed, A.: A real-time hourly ozone prediction system using deep convolutional neural network, *Neural Comput. Appl.*, 32, 8783–8797, <https://doi.org/10.1007/s00521-019-04282-x>, 2020.
- Fleming, Z. L., Doherty, R. M., Von Schneidemesser, E., Malley, C. S., Cooper, O. R., Pinto, J. P., Colette, A., Xu, X., Simpson, D., Schultz, M. G., Lefohn, A. S., Hamad, S., Moolla, R., Solberg, S., and Feng, Z.: Tropospheric Ozone Assessment Report: Present-day ozone distribution and trends relevant to human health, *Elem. Sci. Anth.*, 6, 12, <https://doi.org/10.1525/elementa.273>, 2018.
- Fuentes, M. and Raftery, A. E.: Model Evaluation and Spatial Interpolation by Bayesian Combination of Observations with Outputs from Numerical Models, *Biometrics*, 61, 36–45, <https://doi.org/10.1111/j.0006-341X.2005.030821.x>, 2005.
- Gardner, M. and Dorling, S.: Artificial Neural Network-Derived Trends in Daily Maximum Surface Ozone Concentrations, *J. Air Waste Ma.*, 51, 1202–1210, <https://doi.org/10.1080/10473289.2001.10464338>, 2001.
- Grell, G. A., Peckham, S. E., Schmitz, R., McKeen, S. A., Frost, G., Skamarock, W. C., and Eder, B.: Fully coupled “online” chemistry within the WRF model, *Atmos. Environ.*, 39, 6957–6975, <https://doi.org/10.1016/j.atmosenv.2005.04.027>, 2005.
- Horowitz, J. and Barakat, S.: Statistical analysis of the maximum concentration of an air pollutant: Effects of autocorrelation and non-stationarity, *Atmos. Environ.*, 13, 811–818, [https://doi.org/10.1016/0004-6981\(79\)90272-5](https://doi.org/10.1016/0004-6981(79)90272-5), 1979.
- Horowitz, L. W., Stacy, W., Mauzerall, D. L., Emmons, L. K., Rasch, P. J., Granier, C., Tie, X., Lamarque, J., Schultz, M. G., Tyndall, G. S., Orlando, J. J., and Brasseur, G. P.: A global simulation of tropospheric ozone and related tracers: Description and evaluation of MOZART, version 2, *J. Geophys. Res.-Atmos.*, 108, D12, <https://doi.org/10.1029/2002JD002853>, 2003.
- Ioffe, S. and Szegedy, C.: Batch Normalization: Accelerating Deep Network Training by Reducing Internal Covariate Shift, *arXiv [preprint]*, *arXiv:1502.03167*, 2015.
- Ismail Fawaz, H., Forestier, G., Weber, J., Idoumghar, L., and Muller, P.-A.: Deep learning for time series classification: a review, *Data Min. Knowl. Disc.*, 33, 917–963, <https://doi.org/10.1007/s10618-019-00619-1>, 2019.
- Jacobson, M. Z.: Fundamentals of Atmospheric Modeling, Cambridge University Press, Cambridge, UK, 2005.
- Jülich Supercomputing Centre: JUWELS: Modular Tier-0/1 Supercomputer at Jülich Supercomputing Centre, *Journal of large-scale research facilities*, 5, A135, <https://doi.org/10.17815/jlsrf-5-171>, 2019.
- Kingma, D. P. and Ba, J.: Adam: A Method for Stochastic Optimization, *arXiv [preprint]*, *arXiv:1412.6980*, 2014.
- Kleinert, F., Leufen, L. H., and Schultz, M. G.: IntelliO3-ts: Data, b2share, <https://doi.org/10.34730/c5dae21fac954aa6bdb4e86172221526>, 2020a.
- Kleinert, F., Leufen, L. H., and Schultz, M. G.: IntelliO3-ts: Source code and data, https://doi.org/10.23728/b2share.5042cda41a4c49769cc4010d231ecdec_b2share, 2020b.
- LeCun, Y., Bottou, L., Bengio, Y., and Haffner, P.: Gradient-based learning applied to document recognition, in: *Proceedings of the IEEE*, 86, 2278–2324, <https://doi.org/10.1109/5.726791>, 1998.
- Lefohn, A. S., Malley, C. S., Simon, H., Wells, B., Xu, X., Zhang, L., and Wang, T.: Responses of human health and vegetation exposure metrics to changes in ozone concentration distributions in the European Union, United States, and China, *Atmos. Environ.*, 152, 123–145, <https://doi.org/10.1016/j.atmosenv.2016.12.025>, 2017.
- Liu, B., Yan, S., Li, J., Qu, G., Li, Y., Lang, J., and Gu, R.: A Sequence-to-Sequence Air Quality Predictor Based on the n-Step Recurrent Prediction, *IEEE Access*, 7, 43331–43345, <https://doi.org/10.1109/ACCESS.2019.2908081>, 2019.
- Ma, J., Li, Z., Cheng, J. C., Ding, Y., Lin, C., and Xu, Z.: Air quality prediction at new stations using spatially transferred bi-directional long short-term memory network, *Sci. Total Environ.*, 705, 135771, <https://doi.org/10.1016/j.scitotenv.2019.135771>, 2020.
- Maleki, H., Sorooshian, A., Goudarzi, G., Baboli, Z., Tahmasebi Birgani, Y., and Rahmati, M.: Air pollution prediction by using an artificial neural network model, *Clean Technol. Environ.*, 21, 1341–1352, <https://doi.org/10.1007/s10098-019-01709-w>, 2019.
- Met Office: Cartopy: a cartographic python library with a Matplotlib interface, Exeter, Devon, available at: <https://scitools.org.uk/cartopy> (last access: 18 December 2020), 2010–2015.
- Mills, G., Sharps, K., Simpson, D., Pleijel, H., Broberg, M., Udling, J., Jaramillo, F., Davies, W. J., Dentener, F., Van den Berg, M., Agrawal, M., Agrawal, S., Ainsworth, E. A., Büker, P., Emberson, L., Feng, Z., Harmens, H., Hayes, F., Kobayashi, K., Paoletti, E., and Van Dingenen, R.: Ozone pollution will compromise efforts to increase global wheat production, *Glob. Change Biol.*, 24, 3560–3574, <https://doi.org/10.1111/gcb.14157>, 2018.

- Murphy, A. H.: Skill Scores Based on the Mean Square Error and Their Relationships to the Correlation Coefficient, *Mon. Weather Rev.*, 116, 2417–2424, [https://doi.org/10.1175/1520-0493\(1988\)116<2417:SSBOTM>2.0.CO;2](https://doi.org/10.1175/1520-0493(1988)116<2417:SSBOTM>2.0.CO;2), 1988.
- Murphy, A. H. and Winkler, R. L.: A General Framework for Forecast Verification, *Mon. Weather Rev.*, 115, 1330–1338, [https://doi.org/10.1175/1520-0493\(1987\)115<1330:AGFFV>2.0.CO;2](https://doi.org/10.1175/1520-0493(1987)115<1330:AGFFV>2.0.CO;2), 1987.
- Murphy, A. H., Brown, B. G., and Chen, Y.-S.: Diagnostic Verification of Temperature Forecasts, *Weather Forecast.*, 4, 485–501, [https://doi.org/10.1175/1520-0434\(1989\)004<0485:DVOTF>2.0.CO;2](https://doi.org/10.1175/1520-0434(1989)004<0485:DVOTF>2.0.CO;2), 1989.
- Olszyna, K., Luria, M., and Meagher, J.: The correlation of temperature and rural ozone levels in southeastern USA, *Atmos. Environ.*, 31, 3011–3022, [https://doi.org/10.1016/S1352-2310\(97\)00097-6](https://doi.org/10.1016/S1352-2310(97)00097-6), 1997.
- Pawlak, I. and Jarosławski, J.: Forecasting of Surface Ozone Concentration by Using Artificial Neural Networks in Rural and Urban Areas in Central Poland, *Atmosphere*, 10, 52, <https://doi.org/10.3390/atmos10020052>, 2019.
- Prybutok, V. R., Yi, J., and Mitchell, D.: Comparison of neural network models with ARIMA and regression models for prediction of Houston's daily maximum ozone concentrations, *Eur. J. Oper. Res.*, 122, 31–40, [https://doi.org/10.1016/S0377-2217\(99\)00069-7](https://doi.org/10.1016/S0377-2217(99)00069-7), 2000.
- Rasp, S. and Lerch, S.: Neural Networks for Postprocessing Ensemble Weather Forecasts, *Mon. Weather Rev.*, 146, 3885–3900, <https://doi.org/10.1175/MWR-D-18-0187.1>, 2018.
- Roeder, L.: Netron, github, available at: <https://github.com/lutzroeder/netron>, last access: 18 December 2020.
- Sayeed, A., Choi, Y., Eslami, E., Lops, Y., Roy, A., and Jung, J.: Using a deep convolutional neural network to predict 2017 ozone concentrations, 24 hours in advance, *Neural Networks*, 121, 396–408, <https://doi.org/10.1016/j.neunet.2019.09.033>, 2020.
- Schmidhuber, J.: Deep learning in neural networks: An overview, *Neural Networks*, 61, 85–117, <https://doi.org/10.1016/j.neunet.2014.09.003>, 2015.
- Schultz, M. G., Schröder, S., Lyapina, O., Cooper, O., Galbally, I., Petropavlovskikh, I., Von Schneidmesser, E., Tanimoto, H., Elshorbany, Y., Naja, M., Seguel, R., Dauert, U., Eckhardt, P., Feigenspahn, S., Fiebig, M., Hjellbrekke, A.-G., Hong, Y.-D., Christian Kjeld, P., Koide, H., Lear, G., Tarasick, D., Ueno, M., Wallasch, M., Baumgardner, D., Chuang, M.-T., Gillett, R., Lee, M., Molloy, S., Moolla, R., Wang, T., Sharps, K., Adame, J. A., Ancellet, G., Apadula, F., Artaxo, P., Barlasina, M., Bogucka, M., Bonasoni, P., Chang, L., Colomb, A., Cuevas, E., Cupeiro, M., Degorska, A., Ding, A., Fröhlich, M., Frolova, M., Gadhavi, H., Gheusi, F., Gilge, S., Gonzalez, M. Y., Gros, V., Hamad, S. H., Helmig, D., Henriques, D., Hermansen, O., Holla, R., Huber, J., Im, U., Jaffe, D. A., Komala, N., Kubistin, D., Lam, K.-S., Laurila, T., Lee, H., Levy, I., Mazzoleni, C., Mazzoleni, L., McClure-Begley, A., Mohamad, M., Murovic, M., Navarro-Comas, M., Nicodim, F., Parrish, D., Read, K. A., Reid, N., Ries, L., Saxena, P., Schwab, J. J., Scorgie, Y., Senik, I., Simmonds, P., Sinha, V., Skorokhod, A., Spain, G., Spangl, W., Spoor, R., Springston, S. R., Steer, K., Steinbacher, M., Suharguniyawan, E., Torre, P., Trickl, T., Weili, L., Weller, R., Xu, X., Xue, L., and Zhiqiang, M.: Tropospheric Ozone Assessment Report: Database and Metrics Data of Global Surface Ozone Observations, *Elementa*, 5, 58, <https://doi.org/10.1525/elementa.244>, 2017.
- Seabold, S. and Perktold, J.: Statsmodels: Econometric and statistical modeling with python, in: *Proceedings of the 9th Python in Science Conference*, 28 June–3 July, Austin, Texas, 92–96, <https://doi.org/10.25080/Majora-92bf1922-011>, 2010.
- Seinfeld, J. H. and Pandis, S. N.: *Atmospheric Chemistry and Physics: From Air Pollution to Climate Change*, Wiley, Hoboken, New Jersey, USA, 2016.
- Seltzer, K. M., Shindell, D. T., Kasibhatla, P., and Malley, C. S.: Magnitude, trends, and impacts of ambient long-term ozone exposure in the United States from 2000 to 2015, *Atmos. Chem. Phys.*, 20, 1757–1775, <https://doi.org/10.5194/acp-20-1757-2020>, 2020.
- Silva, S. J., Heald, C. L., Ravela, S., Mammarella, I., and Munger, J. W.: A Deep Learning Parameterization for Ozone Dry Deposition Velocities, *Geophys. Res. Lett.*, 46, 983–989, <https://doi.org/10.1029/2018GL081049>, 2019.
- Srivastava, N., Hinton, G., Krizhevsky, A., Sutskever, I., and Salakhutdinov, R.: Dropout: a simple way to prevent neural networks from overfitting, *J. Mach. Learn. Res.*, 15, 1929–1958, 2014.
- Szegedy, C., Liu, W., Jia, Y., Sermanet, P., Reed, S., Anguelov, D., Erhan, D., Vanhoucke, V., and Rabinovich, A.: Going deeper with convolutions, in: *Proceedings of the 2015 IEEE Conference on Computer Vision and Pattern Recognition (CVPR)*, Boston, MA, USA, 7–12 June 2015, 1–9, <https://doi.org/10.1109/CVPR.2015.7298594>, 2015.
- Thompson, M. L., Reynolds, J., Cox, L. H., Guttorp, P., and Sampson, P. D.: A review of statistical methods for the meteorological adjustment of tropospheric ozone, *Atmos. Environ.*, 35, 617–630, [https://doi.org/10.1016/S1352-2310\(00\)00261-2](https://doi.org/10.1016/S1352-2310(00)00261-2), 2001.
- US Environmental Protection Agency: Technical Assistance Document for the Reporting of Daily Air Quality – the Air Quality Index (AQI), available at: <https://www.airnow.gov/sites/default/files/2018-05/aqi-technical-assistance-document-may2016.pdf> (last access: 18 December 2020), 2016.
- Vautard, R.: Evaluation of the meteorological forcing used for the Air Quality Model Evaluation International Initiative (AQMEII) air quality simulations, *Atmos. Environ.*, 53, 15–37, <https://doi.org/10.1016/j.atmosenv.2011.10.065>, 2012.
- von Kuhlmann, R., Lawrence, M. G., Crutzen, P. J., and Rasch, P. J.: A model for studies of tropospheric ozone and nonmethane hydrocarbons: Model description and ozone results, *J. Geophys. Res.-Atmos.*, 108, D9, <https://doi.org/10.1029/2002JD002893>, 2003.
- Wang, Y., Jacob, D. J., and Logan, J. A.: Global simulation of tropospheric O₃-NO_x-hydrocarbon chemistry: 1. Model formulation, *J. Geophys. Res.-Atmospheres*, 103, 10713–10725, <https://doi.org/10.1029/98JD00158>, 1998a.
- Wang, Y., Logan, J. A., and Jacob, D. J.: Global simulation of tropospheric O₃-NO_x-hydrocarbon chemistry: 2. Model evaluation and global ozone budget, *J. Geophys. Res.-Atmos.*, 103, 10727–10755, <https://doi.org/10.1029/98JD00157>, 1998b.
- WHO: Health risks of air pollution in Europe – HRAPIE project, Recommendations for concentration-response functions for cost-benefit analysis of particulate matter, ozone and nitrogen dioxide, Technical Report, WHO Regional Office for Europe, Copenhagen, Denmark, available at:

- http://www.euro.who.int/__data/assets/pdf_file/0006/238956/Health_risks_air_pollution_HRAPIE_project.pdf?ua=1, (last access: 18 December 2020), 2013.
- Wilks, D. S.: Statistical methods in the atmospheric sciences, International Geophysics Series, Elsevier, USA, UK, ISBN 978-0-12-751966-1, 2006.
- Yan, Y., Pozzer, A., Ojha, N., Lin, J., and Lelieveld, J.: Analysis of European ozone trends in the period 1995–2014, *Atmos. Chem. Phys.*, 18, 5589–5605, <https://doi.org/10.5194/acp-18-5589-2018>, 2018.
- Zhang, Q., Lam, J. C., Li, V. O., and Han, Y.: Deep-AIR: A Hybrid CNN-LSTM Framework for Fine-Grained Air Pollution Forecast, *arXiv [preprint]*, arXiv:2001.11957, 2020.